

ENERGY AND PARTICLE TECHNOLOGY GROUP

RESEARCH GROUP AT MECHANICAL ENGINEERING DEPARTMENT
CARLETON UNIVERSITY

Designing a Common Platform for Modelling Soot in Flames and Reactors

Supervisor: Dr. Reza Kholghy

Author:

Mo ADIB
Carleton University
mo.adib@carleton.ca

Reviewer:

Reza KHOLGHY
reza.kholghy@carleton.ca

Disclaimer: This is a student progress work, done as part of a research assistantship. Any reader should be aware that it might not be free of errors. Still, it might be useful for someone who would like learn some details similar to the ones presented in the report and in the accompanying files.

The material has gone through a review process by group's supervisor.

Last time updated on:

January 9, 2024

Contents

1	Introduction	5
1.1	Motivation	5
1.2	Background	6
1.2.1	Soot inception and surface growth	6
2	Theoretical Model	10
2.1	Assumptions and conventions	10
2.2	Flames	11
2.3	Reactors	12
2.3.1	Constant Volume Reactor	12
2.3.2	Perfectly Stirred Reactor	13
2.3.3	Plug Flow Reactor	14
2.4	Particle Dynamics	15
2.4.1	Soot Morphology	15
2.4.2	Diffusion of soot particles	16
2.4.3	Soot Composition	17
2.4.4	Monodisperse Population Balance Model	17
2.4.4.1	Coagulation	17
2.4.4.2	Source terms	18
2.4.5	Sectional Population Balance Model	18
2.4.5.1	Coagulation	19
2.4.5.2	Source terms	20
2.5	Surface reactions model	22
2.6	PAH growth models	24
2.6.1	Irreversible Dimerization	25
2.6.2	Reactive Dimerization	26
2.6.3	Dimer Coalescence	28
2.6.4	E-Bridge Formation	30
2.7	Gas scrubbing rates	32
3	Results	33
3.1	Validation	33
3.1.1	Collision Frequency	33
3.1.2	Coagulation	34
3.1.3	Constant Volume Reactor	34
3.1.4	Plug Flow Reactor	36
3.2	Burner-stabilized Premixed Flames	36
3.3	Shock-tubes	36

A	Derivation of Transport Equations	54
A.1	Constant Volume Reactor	54
A.1.1	Continuity	54
A.1.2	Species	54
A.1.3	Energy	55
A.1.4	Soot Variables	56
A.2	Plug Flow Reactor	57
A.2.1	Continuity	57
A.2.2	Species	57
A.2.3	Energy	58
A.3	Perfectly Stirred Reactor	59
A.3.1	Continuity	59
A.3.2	Species	59
A.3.3	Energy	60

Nomenclature

Acronyms

CFD	Computational Fluid Dynamics
DEM	Discrete Element Modelling
HACA	Hydrogen abstraction carbon addition
MPBM	Monodisperse Population Balance Model
SPBM	Sectional Population Balance Model

Constants

A_v	Avogadro's number	$6.02214076 \times 10^{23} \text{ 1/mol}$
k_B	Boltzmann constant	$1.3806488 \times 10^{-23} \text{ m}^2\text{kg/s}^2\text{-K}$

English symbols

C_{tot}	Total carbon content of soot particles (per section)	mol/kg
D	Diffusion coefficient of particles	m^2/s
d	diameter	m
d_c	Collision diameter	m
d_g	Gyration diameter	m
d_m	Mobility diameter	m
d_p	Primary particle diameter	m
H_{tot}	Total hydrogen content of soot particles (per section)	mol/kg
I	Source terms for soot variables	$\text{mol}/(\text{kg} \cdot \text{s})$
k	reaction rate constant	$\text{m}^3/(\text{mol} \cdot \text{s})$
m	mass	kg
n_p	Number of primary particles of per agglomerate	
N_{agg}	Number density of agglomerates	mol/kg
N_{pri}	Number density of primary particles	mol/kg
SF	Sectional spacing factor	—
T	Temperature	K
W	Molecular weight	kg

Greek symbols

β	Collision frequency	m^3/s
δ_a	Mean distance of particles	m
λ	Mean free path	m
λ_a	Mean stopping distance of particles	m
ν	Gas kinematic viscosity	m^2/s
ρ	Gas density	kg/m^3
ρ_{soot}	Soot density	kg/m^3
φ	Soot volume fraction	m^3/m^3

Subscripts

ads	Adsorption
agg	Agglomerate
coag	Coagulation
cont	Continuum
f	forward
fm	Free molecular
g	Gyration
grow	Surface growth
inc	Inception
m	Mobility
ox	Oxidation
pri	Primary particle
r	reverse
reac	reactive

Chapter 1

Introduction

1.1 Motivation

Carbonaceous nanoparticles, such as Carbon Black (CB) and soot, are widely encountered in nature and engineering. Every year, nearly 9.5 megatons of soot (black carbon) is emitted into the atmosphere from anthropogenic activities and natural sources such as wildfires and volcanoes [1]. The wide light absorption range of soot reduces the albedo of snow-covered area and alters the radiative forcing balance in the atmosphere making soot the third strongest contributor to climate change after methane and carbon dioxide [1]. Also, exposure to combustion-generated soot could promote respiratory and cardiovascular disease [2]. So, strict regulations are targeting combustion engines to limit environmental and health risks from soot formation [3]. Accurate and affordable models are essential for the prediction of soot composition and morphology in combustion devices and help to reduce the emissions in engines. They can also provide better understanding of soot optical properties that are major indicator of soot environmental effects.

On the other hand, CB with a similar synthesis process and structure to soot but higher elemental carbon to hydrogen ratios ($>97\%$) [4] is commercially produced and sold in large scales. In fact, CB is the largest industrially produced nanomaterial by value and volume (~ 15 megatons per year with a value of \$17B) with applications as a reinforcing agent in rubber and tire industries [5] and conductive additive in lithium-ion batteries [6]. Carbon Black is primarily manufactured by the so-called furnace process where about 50% of heavy fuel oil is partially combusted to convert the rest of it into CB [7]. This process suffers from low mass yield and excessive emission, generating 4 tons of CO_2 per each ton of product on average [8]. Plasma reactor is an emerging alternative production method with distinct advantages over flame-based methods: They can achieve 100% carbon yields with no direct CO_2 emission or other pollutants such, SO_x or NO_x [9], and the energy required for pyrolysis is supplied by an electric arc that does not depend on the feedstock composition. Controlling CB properties such as its specific surface area (or primary particle diameter), hard agglomerate size (or gyration diameter of agglomerates with primary particles connected to each other by strong chemical bonds), and composition (or particle carbon to hydrogen ratio) is important to make process economical and to achieve specific grades of CB for different target applications. However, this is a challenging task because of the complexity of CB formation and mass growth processes and its coupling with gas phase chemistry, dependence on local temperature and pressure. This requires accurate process design and optimization tools that provides insight into CB formation and evolution process, and inform manufacturer's decisions to adjust to produce CB with desired grades [10].

The term "*soot*" usually refers to unwanted particulate matter formed during incomplete combustion of any carbon-containing material from jet and diesel fuel to wood, heavy oil, and plastics with variable organic content and large H/C ratios [4], but this research focuses on soot particles generated under controlled laboratory conditions from fuels with known compositions. The mature soot formed in methane and ethylene premixed flame can reach 95% elemental C/H ratio [11], which is close to CB composition. The comparison of the TEM images of industrially produced

CB [12] with soot from diesel fuel [13, 14] indicates similarity of their morphology and structure. Hereafter, soot is used to describe carbonaceous nanoparticles produced in flame/reactor during combustion/pyrolysis.

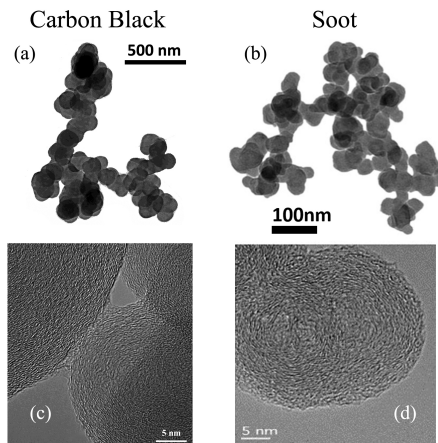


Figure 1.1: The TEM images of Carbon black (a & c) [12] and soot (b & d) [13, 14] that shows soot and CB has similar morphology and structure

1.2 Background

1.2.1 Soot inception and surface growth

Soot formation is a complex process which involves gas phase chemistry, gas-to-solid transition, heterogeneous reactions on solid particles, and aerosol dynamics [15]. It starts with inception which refers to the birth of "incipient" soot particles. The elementary reactions leading to soot inception are still elusive due to coupling with gas chemistry [16], dependence on local temperature [17] and pressure [18]. It has also been challenging to pinpoint the start of inception because of its short time scales in the order 10^{-9} s [19], the lack of a decisive criterion to distinguish molecules from particles [15], and the overlap of inception with particle growth and agglomeration [20]. Despite these limitations and challenges, our knowledge about soot formation has significantly increased thanks to advances in diagnostics methods and reaction mechanism development.

There is compelling evidence that highlights the role of Polycyclic Aromatic Hydrocarbons (PAH) as the main soot precursors. They are thermodynamically stable enough to withstand dissociation at high flame temperatures [21] and observed in stacked layers in High Resolution Transmission Electron Microscope (HRTEM) images of soot primary particles [22].

[placeholder for literature review on the role of diradicals and resonantly stabilized radicals in soot inception]

But, the two important questions need to be answered: (1) which PAHs contribute most to the inception, and (2) what pathways best describe PAH to incipient soot transition. Purely chemical growth mechanisms are shown to underpredict inception rates and particle size [?]. The bimodality of particle size distribution in premixed flames [23] suggests a mechanism second order with respect to the monomer [16]. To satisfy these requirements, a collision-based inception was proposed where irreversible polymerization form PAH clusters held together by Van der Waals forces. The theory postulates that PAH growth continues to reach a certain mass threshold that marks emergence of solid particles, but for practical purposes, a dimer is usually considered as incipient soot.

In this model, hereafter referred to as **Irreversible Dimerization**, the collision of two PAH molecules is assumed to form a dimer. Irreversible Dimerization has been used to predict soot formation in burner-stabilized premixed [24, 25], counterflow diffusion flames [26, 27], coflow diffusion flames [28, 29]. A collision efficiency factor ranging between 10^{-6} to 1 is also employed to adjust

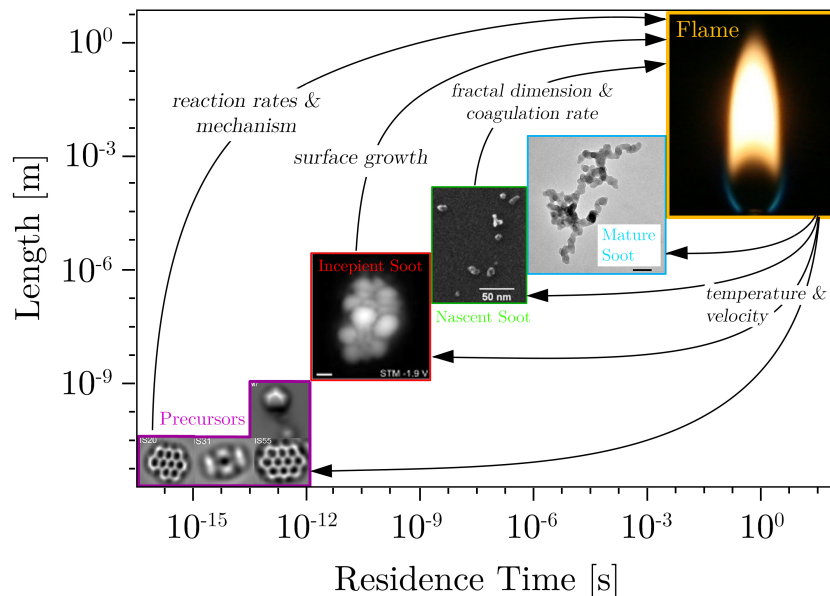


Figure 1.2: The range of time and length scales of the processes involved in soot formation from molecular reactions to particle-fluid interaction in flames

the inception flux and PAH adsorption rates to achieve desired soot mass and size distribution. PAHs of moderate sizes such as pyrene (4 rings) to coronene (7 rings) have been considered as the starting point of inception due to their thermodynamic instability that justifies the irreversibility at high temperatures [30]. Blanquart and Pitsch [31] introduced a two-step process. However, the theoretical calculations [32] and experiments [33] indicated that pyrene dimerization is highly reversible in flame condition.

The inception rate of irreversible dimerization is mainly controlled by PAH concentration due to weak temperature dependency, so it produces new particle in low temperatures (even less than 500 K) [34] despite experimental evidence for termination of inception below 1200 K [35, 36]. Also, the arbitrary selection of efficiency factors alters the distribution of mass between inception and surface growth, which could significantly change soot mass, PSD, and morphology strongly [37]. Miller [38] used equilibrium constant for PAH dimerization to calculate the net dimerization rate and demonstrated that the collision of PAHs larger than circumvalene (~ 800 amu) could last long enough to grow into incipient soot. However, the concentration of PAHs drops rapidly with size [16]. The entropy barrier of dimerization is significant for larger PAHs [39].

Eaves et al. [40] relaxed the irreversibility assumption, and developed a reversible clustering model to simulate inception using an array of PAHs from naphthalene to benzo-pyrene. Building on that work, Kholghy et al. [41] emphasized on the necessity of chemical bond formation after physical PAH clustering for accurate prediction of volume fraction, primary particle diameter and PSD in ethylene coflow diffusion flames. Later, Kholghy et al. [42] proposed the "Reactive Dimerization" model which starts with reversible collision of PAHs leading to physical dimers held with vdW forces that are graphitized and form chemically-bonded dimer that serve as soot nuclei and grow via surface reactions. They also performed a systematic analysis on contribution of different PAHs, and concluded that one- and two-ring aromatics account for almost all of inception flux in the so-called "sooting flame" [25]. However, Frenklach and Mebel [43] pointed out that an inception model that initiated with a highly reversible step similar to Reactive Dimerization [42] cannot produce sufficient flux of particles to match measurements of the benchmark burner-stabilized stagnation flame [44]. Instead, they proposed a HACA-driven mechanism where addition of monomer molecule to its radical activated by hydrogen abstraction for a stable dimer via an E-Bridge bond formation, and this sequential process continues to form trimers, tetramers, and larger PAH clusters.

After inception, soot particles grow by the addition of small hydrocarbon species to their surface. This process is described by the famous hydrogen–abstraction–acetylene–addition (HACA) mechanism [30, 45] that assumes the soot surface to consist of hydrogenated sites with a predefined density. Mass growth on soot surface requires H-abstraction to form a radical site, followed by acetylene attack similar to growth of PAH molecules in the gas-phase. The reactivity of these sites depends on with time and temperature [46, 47]. However, soot mass growth without the presence of H radicals [48] indicated the incompleteness of the HACA mechanism to describe the entire process of soot surface growth.

Adsorption of PAHs on the surface of soot particles is also a viable growth mechanism [30], more specifically called physisorption or chemisorption depending on the mechanisms driving the adsorption process [49]. There is still debate over the stability of adsorbed PAH molecules on soot surface [50]. Following the hypothesis that PAHs are building blocks of soot particles, a mechanism similar to inception is often used to describe PAH-soot growth.

In typical soot formation processes such as flames and reactor, soot particles are formed at high concentrations (10^{12} #/cm^3), and inception and surface growth are relatively short compared to the total residence of soot particles. As a result, coagulation becomes dominant rapidly attaining both [51] self-preserving size distribution (SPSD) [52] and asymptotic fractal-like structure [53]. The evolving fractal-like structure of agglomerates quantified by their mobility diameter normalized by primary particle, d_m/d_p , and gyration, d_m/d_g , diameters can be described with power laws derived from mesoscale simulations [54]. The collision frequency of agglomerates depends on their evolving fractal-like morphology. Also, polydisperse agglomerates collide more frequently than monodisperse ones. The enhancement in their collision frequency reaches an asymptotic value of 35% [51] or 82% [55] in the free molecular or transition regimes, respectively at SPSPD regardless of the polydispersity in their constituent primary particles. Particle morphology formed by inception, surface growth and agglomeration can be tracked precisely by mesoscale simulations, such as Discrete Element Modeling (DEM) [56]. However, they are computationally expensive and interfacing them with chemical kinetics in computational fluid dynamics (CFD) simulations is not trivial [57]. This limits their application. So, sectional population balance models (SPBM) are often used to track agglomerate and primary particle size distribution [58], morphology [59], and composition [28] in complex laminar [28] and turbulent flows [60]. Using the SPBMs coupled with relations for agglomerate fractal-like structure [61] and collision frequency [36], particle size distribution, morphology and composition can be tracked accurately. However, the computational cost of SPBMs increases exponentially with the number of sections [31] and particle properties [28] tracked. Thus, one property (e.g. agglomerate mass) is typically tracked with SPBMs to reduce computational cost. This does not allow to account for agglomerate fractal-like structure [62, 63] which limits SPBM accuracy in predicting surface growth and coagulation rate of agglomerates and their size distribution.

Alternatively, particle dynamics can be tracked by the method of moments (MOM) [64] or monodisperse population balance models (MPBM) [65]. Such models only track average particle properties (e.g. moment ratios) and their accuracy could be limited if unrealistic assumptions (e.g. approximating agglomerates as monodisperse and perfect spheres) are used. However, when inception and surface growth are short [66] and high particle (number) concentrations are formed [54], they lead to rapid attainment of self-preserving size distributions (SPSD) and agglomerates having asymptotic structure [51]. In this case a MPBM or MOM can be assembled on a firm scientific basis with accuracy on par with DEM [56], SPBM [67] and experimental data [68, 69, 23]. Such models can be readily interfaced with CFD simulations [70] without significant computational cost, making them ideal for three-dimensional and even turbulent flame simulations.

The MOM tracks moments of the PSD and estimates average particle properties such as mass [71], surface area [72], the number of constituent primary particles per agglomerate, n_p [64], or even particle composition [31] using the ratio of the moments. The MOM with four equations was used to describe synthesis of optical fibers by simultaneous reaction, diffusion, coagulation and thermophoresis of SiO_2 in laminar flow reactors assuming a lognormal PSD [73]. The MOM with interpolative closure (MOMIC) was developed to predict simultaneous nucleation, surface growth and coagulation of soot agglomerates and estimate its PSD with six equations [64]. To calculate source terms of the transported moments, additional moments that are not tracked are needed preventing the closure of

the system of differential equations with the MOM [71, 74]. Thus, often the PSD shape is assumed a priori [71] or extra equations are solved to estimate it [65].

The MPBMs do not have the closure problem and calculate average particle properties by tracking their total concentration, mass [65] and area [75, 76]. Kruis et al. [65] used a 2-equation MPBM (known as the semi-empirical model) to track soot concentration and mass in (non-premixed) flames assuming spherical particles. Good agreement was achieved for measured soot mass. However, the specific surface area [76] and coagulation frequency of spheres are significantly smaller compared to that of agglomerates with the same mass underestimating their oxidation rate [67] and overestimating their concentration [40]. Kruis et al. [65] proposed a 3-equation MPBM to account for the fractal-like structure of nanoparticle agglomerates during coagulation and sintering. Agglomerate volume and area were used to obtain their equivalent primary particle diameter, d_p , and n_p . Then, agglomerate collision diameter, i.e. d_g , was calculated by D_f , d_p and n_p to account for their fractal-like structure that affects their collision frequency. Tsantilis and Pratsinis [75] extended the MPBM to predict hard-(chemically-bonded) and soft- (physically-bonded) agglomerates during synthesis of SiO_2 and TiO_2 [77] nanoparticles with simultaneous reaction, surface growth, coagulation and sintering. Such a MPBM applies best at high concentrations when inception and surface growth are short [66] resulting in the dominance of coagulation where particles rapidly reach their SPSSD and asymptotic fractal-like structure. This is often the case for soot emitted from a variety of combustion devices or CB reactors where inception and surface growth are limited to only a few milliseconds when temperature is very high (i.e. $T \geq 1500\text{K}$) [42].

Chapter 2

Theoretical Model

In this chapter, the mathematical basis of *omnisoot* is explained in top-to-bottom hierarchical order. The highest level is the reactors that include the transport equations of gas mixture and "soot variables" for different reactors that relies on the source terms due to soot formation. These source terms are handled by the particle dynamics model that mainly addresses particle size distribution (PSD), morphology and coagulation rate. The "PAH growth model" computes the inception and adsorption based on PAHs designated as precursors, and returns them to the particle dynamics model. Similarly, the "surface reaction" model obtains the surface growth and oxidation rate by HACA schemes and passes them to the particle dynamics model.

2.1 Assumptions and conventions

Here, the main conventions and assumptions used in the derivation of the mathematical model are listed below.

1. \dot{s}_k denotes that rate production/consumption of k_{th} species due to soot formation. It is positive when the species is released to gas mixture.
2. Each soot agglomerate consist of spherical monodisperse primary particles that are in point contact.
3. The word "*particle*" refers to soot both in spherical and agglomerate shape.
4. The density of soot is assumed constant at the value of 1800 kg/m³. This density represents an average between particles with large C/H ratio ($\rho = 1600\text{kg/m}^3$) and small C/H ratios ($\rho = 2000\text{kg/m}^3$) [78].
5. The incipient soot particles are 2 nm in diameter, so no particles could exist with a primary particle diameter smaller than 2 nm. The number of carbon atoms in the incipient soot particle is calculated from the mass of a sphere with the diameter of 2 nm in assuming pure carbon content.

$$\begin{aligned} d_{p,min} &= 2 \text{ nm} \\ n_{c,min} &= \frac{\pi}{6} \rho_{soot} d_{p,min}^3 \frac{1}{MW_c} \approx 378. \end{aligned} \tag{2.1}$$

6. The calculation of PAH adsorption and soot oxidation requires "*soot concentration*" which is defined as number density of soot agglomerates per unit volume of gas. The number density of agglomerates, N_{agg} , are tracked per unit mass of gas mixture i.e. #/kg_{gas}. So, soot concentration can be calculated by multiplying agglomerate number density by gas density as:

$$[\text{soot}] = \rho \cdot N_{agg}. \tag{2.2}$$

7. The specific heat, internal energy and enthalpy of soot are approximated by those of pure graphite, and employed to close the energy balance in the system [79].
8. Soot particles and gas are in thermal equilibrium during all the studied processes, and there is no temperature gradient within each agglomerate.
9. *Soot variable* refers to the features/properties of soot particles tracked by the particle dynamics model and used in the soot transport equations.
10. *PAH growth* is a unit of the soot model with a set of pathways that determine the rate of inception and adsorption from PAHs in the gas mixture.
11. *surface reactions* is a unit of the soot model that describes the addition of acetylene to soot surface, and removal of carbon via oxidation by OH and O2 in the HACA scheme.
12. The superscript i denotes section number of a soot variable or property derived from variables. In the case of the monodisperse model, the section number can be ignored because it is equivalent to the sectional model with one section.
13. The morphological parameters and diffusion coefficient of particles are common between particle dynamics models, so they are explained as two separate sections.

2.2 Flames

This research focuses on flames that can be described by the axisymmetric stagnation flow assumption that reduces the laminar 3D steady-state Navier-Stokes equations in the cylindrical coordinates to one-dimensional domain in r-z plane. A similar approach is applied to the energy and species conservation. The derivation of flow equations for a reacting gas is explained in detail in Section 7.2 of [80]. Here, the modified version of equations is provided that takes into account the mass and momentum of particles, the removal/release of species due to soot inception, surface growth and oxidation as well as the formation and sensible energy of soot.

Continuity:

$$\frac{\partial \rho u}{\partial z} = 2\rho V - \sum_j \dot{s}_j W_j, \quad (2.3)$$

Radial Momentum:

$$\rho u \frac{\partial V}{\partial z} + \rho V^2 = -\Lambda + \frac{\partial}{\partial z} \left(\mu \frac{\partial V}{\partial z} \right), \quad (2.4)$$

Energy:

$$[(1 - \varphi)\rho c_p + \varphi \rho_{soot} c_{p,soot}] u \frac{\partial T}{\partial z} = \frac{\partial}{\partial z} \left(K \frac{\partial T}{\partial z} \right) - \sum_k^{n_{sp}} J_k \frac{\partial h_k}{\partial z} - \sum_k^{n_{sp}} h_k W_k (\omega_k + \dot{s}_k), \quad (2.5)$$

Species:

$$\rho u \frac{\partial Y_k}{\partial z} = -\frac{\partial J_k}{\partial z} + W_j (\omega_k + \dot{s}_k), \quad (2.6)$$

where $V = v/r$ is the scaled radial velocity, and Λ is the pressure eigenvalue. J_k denotes the diffusive flux of species k that is usually calculated using mixture averaged formulation.

$$J_K^* = -\rho \frac{W_k}{W_T} D'_{km} \frac{\partial X_k}{\partial z}, \quad (2.7)$$

$$J_K = J_K^* - Y_k \sum_{l=1}^{n_{sp}} J_l^*, \quad (2.8)$$

The details of calculation of mixture-averaged diffusive fluxes can be found in the documentation of `GasTransport::getMixDiffCoeffs()`¹ in Cantera [81]. Generic soot variables are treated similar to species, and their transport equations can be written as:

$$\rho u \frac{\partial \psi}{\partial z} = -\frac{\partial}{\partial z} \left(D \frac{\partial \psi}{\partial z} \right) + S_\psi, \quad (2.9)$$

2.3 Reactors

Zero-dimensional reactors are ideal representation of reactive systems typical in industrial applications. The strong mixing in the volume/cross-section allows description of thermal/chemical/hydrodynamic properties of the mixture with a single data-point that evolves in time. This section entails the equations that describes the conservation of mass, momentum (if applicable), species, energy, and soot based on ideal gas assumption for gaseous mixture in three different types of reactors.

2.3.1 Constant Volume Reactor

This reactor assumes that the volume of the system does not change during the process. In the absence of soot, this leads to gas with constant density. However, soot formation converts part of gaseous species to solid particles thereby affecting its volume and density. Note that, continuity, species and energy transport equations only track gas mixture properties. Figure 2.1 illustrates the control volume over the gas mixture targeted by mass and energy balance equations. Any mass converted to solid soot particles leaves the control volume. Mass and energy pass through the control surface around solid particles by soot formation processes and variations in the temperature of the particles. Reactor volume is shared between gas and solid particles.

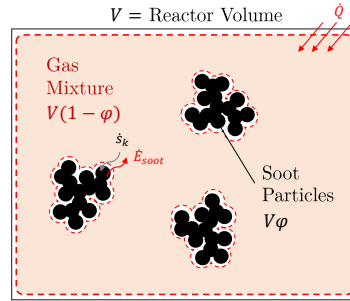


Figure 2.1: The schematics of the control volume considered for the constant volume reactor that encompasses the gas mixture and excludes the soot particles. Mass and energy are transferred between gas and soot particles.

The continuity for this reactor can be written as:

$$\frac{d}{dt}(\rho(1 - \phi)) = (1 - \phi) \sum_i \dot{s}_i W_i. \quad (2.10)$$

Similarly, the species equation for species k is expressed as:

$$\frac{dY_k}{dt} = \frac{\dot{m}_{in}}{\rho V (1 - \phi)} (Y_k^* - Y_k) + \frac{1}{\rho} (\dot{\omega}_k + \dot{s}_k) W_k - \frac{1}{\rho} Y_k \sum_i \dot{s}_i W_i. \quad (2.11)$$

The energy balance for the constant volume reactor considering an external heat source of \dot{Q} can

¹https://cantera.org/documentation/docs-3.0/doxygen/html/d8/d58/classCantera_1_1GasTransport.html

be simplified to the equation that describes the temperature variations.

$$\frac{dT}{dt} = \frac{1}{\rho(1-\varphi)c_v + \rho_{soot}\varphi c_{v,soot}} \left[-(1-\varphi) \sum_k e_k (\dot{\omega}_k + \dot{s}_k) W_k + u_{soot}(1-\varphi) \sum_k \dot{s}_k W_k + \frac{\dot{Q}}{V} \right]. \quad (2.12)$$

The transport equation for a generic soot variable, ψ can be written as:

$$\frac{d\psi}{dt} = S_\psi - \frac{\psi}{\rho} \sum_i \dot{s}_i W_i. \quad (2.13)$$

2.3.2 Perfectly Stirred Reactor

In this reactor, gas enters with a mass flow rate \dot{m}_{in} , composition of Y^* and temperature of T^* , instantaneously mixes and homogeneously reacts with the mixture resident inside the reactor to reach a spatially uniform temperature and composition described by a single T , and Y . It is assumed that temperature, composition and soot properties of the outflow are the same as the reactor. Figure 2.2 illustrates the schematics of PSR. \dot{m}_{in} and \dot{m}_{out} refer to inflow and outflow gas mass flow rates, respectively. Under no-soot conditions, the inlet and outlet mass flow rates are equal, but the gas mixture loses mass by soot formation, so \dot{m}_{out} is slightly less than \dot{m}_{in} . The pressure of the reactor is assumed to stay constant during the process [80]. The nominal residence time of gas mixture in the reactor is defined as:

$$\tau = \frac{\rho V}{\dot{m}_{in}}. \quad (2.14)$$

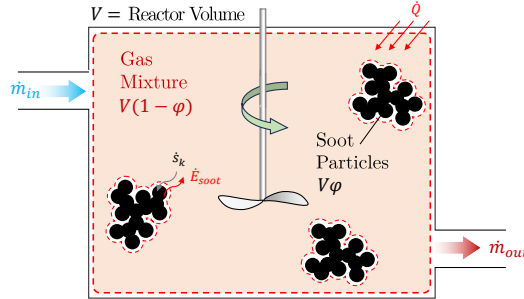


Figure 2.2: The schematics of the control volume considered for the perfectly stirred reactor that encompasses the gas mixture and excludes the soot particles. Mass and energy are transferred between gas and soot particles. The inlet flow brings species and enthalpy into the control volume and the outflow discharges them. The gas mass flow rate reduces due to soot formation.

The conservation of mass can be written for PSR by considering the mass flux of in- and outflow, and the removal of mass due to soot generation as:

$$\frac{dm}{dt} = \dot{m}_{in} - \dot{m}_{out} + (1-\varphi) \sum_i \dot{s}_i W_i. \quad (2.15)$$

The density is not determined by solving the continuity equation, but rather from ideal gas law and assuming a constant pressure and the composition from solving the species transport equations

$$\frac{dY_k}{dt} = \frac{1}{\tau} (Y_k^* - Y_k) + \frac{1}{\rho} \left[(\dot{\omega}_k + \dot{s}_k) W_k - Y_k \sum_i \dot{s}_i W_i \right]. \quad (2.16)$$

The energy equation for this reactor is written as:

$$\frac{dT}{dt} = \frac{1}{\rho(1-\varphi)c_p + \rho_{soot}c_{p,soot}\varphi} \left[\frac{\dot{m}_{in}}{V}(h^* - h) - \frac{\dot{m}_{in}}{V} \sum_k (Y_k^* - Y_k) h_k - (1-\varphi) \sum_k (\dot{\omega}_k + \dot{s}_k) W_k h_k + (1-\varphi) \sum_i \dot{s}_i W_i h_{soot} + \frac{\dot{Q}}{V} \right]. \quad (2.17)$$

The soot transport equations can also be expressed as:

$$\frac{d\psi}{dt} = \frac{\dot{m}_{in}}{\rho V(1-\varphi)} (\psi^* - \psi) + S_\psi - \frac{1}{\rho} \psi \sum_i \dot{s}_i W_i. \quad (2.18)$$

2.3.3 Plug Flow Reactor

The plug flow reactor (PFR) is based on a channel or duct with a constant cross-sectional area where a steady-state one-dimensional flow changes temperature, composition, and soot properties along the channel. There is no spatial gradient over the cross-section due to strong mixing, and diffusion along the channel is negligible. The pressure is assumed constant along the reactor.

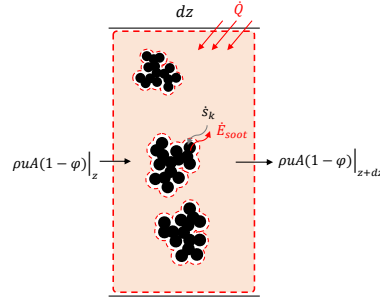


Figure 2.3: The schematics of the control volume for a differential element along PFR that includes the gas mixture and excludes the soot particles considering wall heat transfer. Mass and energy are transferred between gas and soot.

The continuity equation for PFR is written as:

$$\frac{d}{dz}(\rho u(1-\varphi)) = (1-\varphi) \sum_i \dot{s}_i W_i. \quad (2.19)$$

The species equation can be expressed as:

$$\frac{dY_k}{dz} = \frac{1}{\rho u} \left[(\dot{\omega}_k + \dot{s}_k) W_k - Y_k \sum_i \dot{s}_i W_i \right]. \quad (2.20)$$

The energy equation can be expressed as:

$$\frac{dT}{dz} = \frac{1}{\rho u(1-\varphi)c_p + \rho_{soot}u\varphi c_{p,soot}} \left[-(1-\varphi) \sum_k h_k (\dot{\omega}_k + \dot{s}_k) W_k + h_{soot}(1-\varphi) \sum_k \dot{s}_k W_k + \dot{q}' \right]. \quad (2.21)$$

The soot transport equations can also be written as:

$$\frac{d\psi}{dz} = \frac{S_\psi}{u} - \frac{\psi}{\rho u} \sum_i \dot{s}_i W_i. \quad (2.22)$$

2.4 Particle Dynamics

Population balance models rely on the Eulerian description of particles where bulk properties of particle population such as number density, mass or surface area are treated as continuous quantities and tracked by solving scalar transport equations. These methods are computationally cheaper compared with mesoscale models such as DEM, and can be easily interfaced with chemical kinetics in CFD solvers to simulate soot formation in turbulent configurations. Here, we use two particle dynamics models: a monodisperse population balance model (MPBM) based on four variables leading to 4 transport equations in total, and fixed sectional population balance model (SPBM) tracking three variables per section. The total number of transport equations in the sectional model is determined by the number of sections and number of equations solved per section. The first two/three variables in the MPBM/SPBM enables description of number, mass, and evolving fractal-like morphology of soot agglomerates that are necessary to accurately predict collision frequency of agglomerates [82] as well as oxidation and surface growth rates [67]. The last variable tracks the number of hydrogen atoms in agglomerates that allows the model to capture the soot composition, thereby its maturity [28], and surface reactivity [31]. The tracked variables are used to address particle dynamics that includes (i) reconstructing particles morphology by determining characteristic diameters from tracked soot variables, (ii) calculating collision frequency and coagulation source term, (iii) combining the contribution of inception, PAH adsorption, surface growth and oxidation into source terms. First, common features of both particle dynamics models are reviewed. As mentioned before, any parameter with superscript i denotes the section number, which can be ignored/dropped for the MPBM that only has one section. For example, d_m^i can be replaced with d_m .

2.4.1 Soot Morphology

The evolving fractal-like structure of agglomerates are quantified by their mobility diameter normalized by primary particle, d_m/d_p , and gyration, d_m/d_g , diameters can be described with power laws derived from mesoscale simulations. Incipient soot is initially a sphere formed of PAHs with constant density that grows in size by surface reactions and forms agglomerates by coagulation. The collision frequency of particles depends on their evolving fractal structure because they have larger cross-sectional area compared with mass-equivalent spheres [82]. Some simplifying assumptions are made to reconstruct the particle morphology from tracked variables. The primary particles of each agglomerate are similar enough that can be described by mean size and composition. They also stay in point contact during surface growth and agglomeration i.e. the necking is ignored. A universal fractal dimension, $D_f = 1.9$ is used for agglomerates larger than the sphere [83]. The evolving morphology of soot agglomerates by their mobility diameter normalized by primary particle, d_m/d_p , and gyration, d_m/d_g , diameters that are related to the number of primary particles using power-laws derived from DEM simulations [54]. Mobility and gyration diameters are the diameter of a sphere with the same translational and rotational properties of the agglomerate, respectively. The employed power-laws have been shown to describe the morphology of soot from premixed [68], diffusion [84] flames, and diesel engines [85]. Figure 2.4 illustrates the schematics of sample soot agglomerates with 12 primary particles and depicted d_p , d_m , and d_g .

n_p is the number of primary particles in each agglomerate that can be obtained by dividing the number density of primary particles by that of agglomerates of that section,

$$n_p^i = \frac{N_{pri}^i}{N_{agg}^i}. \quad (2.23)$$

Primary particle diameter, d_p , can be obtained from total carbon and number density of primary particles using

$$d_p^i = \left(\frac{6}{\pi} \frac{C_{tot}^i \cdot W_{carbon}}{\rho_{soot}} \frac{1}{N_{pri}^i \cdot Av} \right)^{1/3}. \quad (2.24)$$

The DEM-derived power-laws [54] relate d_m and d_g to d_p and n_p as

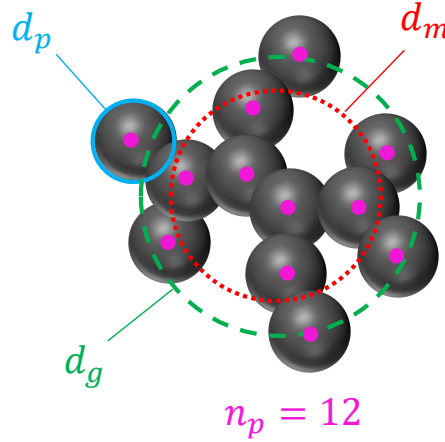


Figure 2.4: The schematics of a soot agglomerates with 12 primary particles ($n_p = 12$). Primary particle (d_p), mobility (d_m), and gyration (d_g) are shown.

$$d_m^i = d_p^i \cdot n_p^{i 0.45}, \quad (2.25)$$

$$d_g^i = \begin{cases} d_m^i / (n_p^{i -0.2} + 0.4), & \text{if } n_p^i > 1.5 \\ d_m^i / 1.29, & \text{if } n_p^i \leq 1.5 \end{cases} \quad (2.26)$$

The collision diameter, d_c^i is the maximum of d_m^i , d_g^i :

$$d_c^i = \max(d_m^i, d_g^i) \quad (2.27)$$

d_m^i , d_g^i , d_c^i are used to calculate the source terms due to the surface growth, oxidation, PAH adsorption and coagulation.

The volume equivalent diameter, d_v^i , is the diameter of the sphere with the same mass as agglomerate, and it is obtained as:

$$d_v^i = d_p^i \cdot n_p^{i 1/3} \quad (2.28)$$

The primary particle surface area is calculated from d_p^i assuming spherical primary particles.

$$A_p^i = \pi d_p^{i 2}, \quad (2.29)$$

A_{tot}^i (for each section) is defined as the total surface area of soot particles per unit mass of gas mixture obtained as

$$A_{tot}^i = N_{pri} A_v \cdot A_p^i. \quad (2.30)$$

2.4.2 Diffusion of soot particles

The diffusion coefficient of soot particle, D^i , is calculated as

$$D^i = \frac{k_B T}{f}, \quad (2.31)$$

where f is the friction factor of particles in gas,

$$f^i = \frac{3\pi\mu d_m^i}{C^i(d_m^i)}, \quad (2.32)$$

where C^i is the Cunningham function that corrects the friction factor given a diameter in the continuum regime for transition and free molecular regimes as:

$$C^i(d) = 1 + \frac{2\lambda}{d} \left(1.21 + 0.4 \cdot \exp\left(\frac{-0.78d}{\lambda}\right) \right), \quad (2.33)$$

where λ is the mean free path of gas given as:

$$\lambda = \frac{\mu}{\rho} \sqrt{\frac{\pi W_{gas}}{2k_B A v T}}. \quad (2.34)$$

Note that, λ is a property of the gas mixture that does not depend on particle morphology and size section. The mean velocity, c^i and mean stop distance of particles, λ_a^i can be calculated as:

$$c^i = \sqrt{\frac{8k_B T}{\pi m_{agg}^i}}. \quad (2.35)$$

$$\lambda_a = \frac{8D^i}{\pi c^i}. \quad (2.36)$$

The mean distance of particles are also calculated as:

$$\delta_a^i = \frac{1}{d_c^i \lambda_a^i} \left[(d_c^i + \lambda_a^i)^3 - (d_c^{i2} + \lambda_a^{i2})^{3/2} \right] - d_{c,j}. \quad (2.37)$$

2.4.3 Soot Composition

The composition of soot is characterized by their elemental carbon to hydrogen ratio (C/H) is a measure of soot maturity and increases from $C/H < 2$ for incipient soot [86] to $2 < C/H < 10$ for nascent soot [87] and $C/H > 20$ for mature soot [88]. The soot agglomerates are assumed to have pure carbon graphitic core [28] with all hydrogen atoms on the surface [31]. C/H ratio can be obtained from total carbon and hydrogen content as:

$$\left(\frac{C}{H} \right)^i = \frac{C_{tot}^i}{H_{tot}^i}. \quad (2.38)$$

The carbon content of each agglomerate is a predefined parameter in the SPBM, but it can be calculated by dividing C_{tot} by N_{agg} for the MPBM. The hydrogen content of each agglomerate is calculated for both particle dynamics models as:

$$H_{agg}^i = \frac{H_{tot}^i}{N_{agg}^i}. \quad (2.39)$$

2.4.4 Monodisperse Population Balance Model

The MPBM used in this research tracks the number density of primary particles (N_{pri}) and agglomerates (N_{agg}), total carbon (C_{tot}) and hydrogen (H_{tot}) content of soot particles per unit mass of gas mixture. The morphological parameters such as primary particle, mobility and gyration diameters obtained from these soot variables are the average values for the population.

2.4.4.1 Coagulation

Coagulation is the process during which solid and hard soot particles collide and attach at point of contact leading to larger agglomerates. This process conserves the soot mass and composition and number density of primary particles, so coagulation only affects N_{agg} . I_{coag}^N accounts for the decay rate of N_{agg} by the binary collision of soot particles by

$$I_{coag} = -\frac{1}{2} \beta N_{agg}^2, \quad (2.40)$$

where β is the collision frequency of agglomerates for the free molecular ($\text{Kn} > 10$) to continuum regime ($\text{Kn} < 0.1$). The value of β in the transition regime ($0.1 < \text{Kn} < 10$) can be calculated from the harmonic mean of the continuum (β_{cont}) and free molecular (β_{fm}) regime values. Additionally, an enhancement factor of 1.82 is applied to take into account the effect of polydispersity [55] as:

$$\beta = 1.82 \frac{\beta_{\text{fm}} \beta_{\text{cont}}}{\beta_{\text{fm}} + \beta_{\text{cont}}}, \quad (2.41)$$

$$\beta_{\text{fm}} = 4 \sqrt{\frac{\pi k_b T}{m_{\text{agg}}}} d_g^2, \quad (2.42)$$

$$\beta_{\text{cont}} = 8\pi d_c D. \quad (2.43)$$

Alternatively, β can be obtained using Fuchs interpolation [89] as:

$$\beta = \beta_{\text{cont}} \left(\frac{d_c}{d_c + 2\sqrt{2}\delta} + \frac{8D}{\sqrt{2}c_r d_c} \right)^{-1}. \quad (2.44)$$

2.4.4.2 Source terms

The source terms of tracked variables combines the effect of the inception, PAH adsorption, surface growth and oxidation and coagulation.

$$S_{N_{\text{agg}}} = \frac{I_{N,\text{inc}}}{n_{c,\text{min}}} + I_{\text{coag}}. \quad (2.45)$$

$$S_{N_{\text{pri}}} = \frac{I_{N,\text{inc}}}{n_{c,\text{min}}}. \quad (2.46)$$

$$S_{C_{\text{tot}}} = I_{C_{\text{tot}},\text{inc}} + I_{C_{\text{tot}},\text{gr}} + I_{C_{\text{tot}},\text{ads}} + I_{C_{\text{tot}},\text{ox}}. \quad (2.47)$$

$$S_{H_{\text{tot}}} = I_{H_{\text{tot}},\text{inc}} + I_{H_{\text{tot}},\text{gr}} + I_{H_{\text{tot}},\text{ads}} + I_{H_{\text{tot}},\text{ox}}. \quad (2.48)$$

The partial source terms in Equations denoted by I are determined by PAH growth and surface reaction model explained in Sections 2.6 and 2.5, respectively.

2.4.5 Sectional Population Balance Model

A SPBM with the fixed pivot is used to describe particle dynamics [90]. The mass range of particles are divided into discrete sections that include agglomerates of the same mass. Inception introduces new particles to the first section with the mass corresponding to the incipient particle. The particles of the first section can migrate to upper sections by gaining mass via surface growth and coagulation, and return to lower sections when they lose mass through oxidation. The mass of sections is determined by a geometric progression with a scale factor equal to the mass of the incipient soot particle, and a common ratio of SF, known as sectional spacing factor. The mass of section is approximated by the carbon content of agglomerates in moles as:

$$C_{\text{agg}}^i = \frac{n_{c,\text{min}}}{A_v} \cdot SF^{i-1}. \quad (2.49)$$

So, the mass of hydrogen is ignored in the placement of agglomerates in the sections. The total number density of agglomerates, N_{agg}^i [mol/kg], and primary particles, N_{pri}^i [mol/kg] are tracked for each section. Morphological parameters are determined for each section according to the equations in Section 2.4.1.

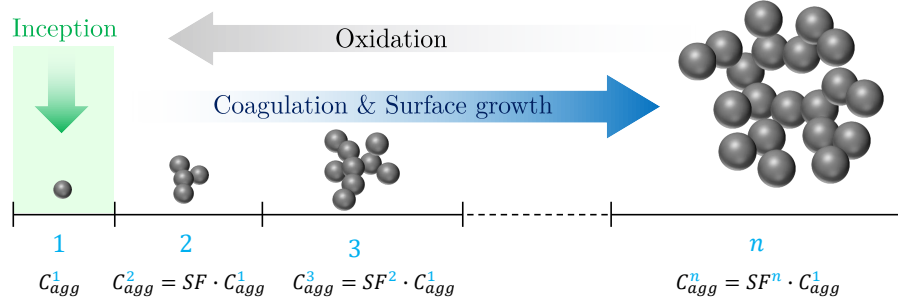


Figure 2.5: The illustration of sections of SPBM. The mass of sections grows progressively by the scale factor of SF. Inception introduces new particles to the first section that propagate to the upper section via coagulation and surface growth and return to lower sections by oxidation

2.4.5.1 Coagulation

In SPBM approach, collisions between particles from every two sections are considered. The new particles formed by coagulation are placed in a upper section with the mass equal to sum of particles involved in the collision. When the mass of yielded particle lies between two consecutive sections, the particles are divided among these sections proportional to their mass. One possible scenario is that the mass of the newly formed particle is greater than the last section, thus leaving tracked mass range. Losing mass is a potential problem with the fixed pivot sectional model, which can be avoided by selecting proper number of sections and spacing factor to ensure the last sections stay empty during the simulation.

The collision frequency between sections j and k can be obtained from the harmonic mean of the values in the continuum and free molecular regimes as:

$$\beta^{jk} = \frac{\beta_{fm}^{jk} \beta_{cont}^{jk}}{\beta_{fm}^{jk} + \beta_{cont}^{jk}}, \quad (2.50)$$

$$\beta_{fm}^{jk} = \sqrt{\frac{\pi k_b T}{2} \left(\frac{1}{m_{agg}^j} + \frac{1}{m_{agg}^k} \right)} (d_c^j + d_c^k)^2, \quad (2.51)$$

$$\beta_{cont}^{ij} = \frac{2k_B T}{3\mu} \left(\frac{C^j}{d_m^j} + \frac{C^k}{d_m^k} \right) (d_c^j + d_c^k)^2. \quad (2.52)$$

The collision frequency can also be determined from the Fuchs interpolation similar to the MPBM as:

$$\beta^{jk} = \beta_{cont}^{ij} \left[\frac{d_c^j + d_c^k}{d_c^j + d_c^k + 2 + \delta_r^{jk}} + \frac{8(D^j + D^k)}{\bar{c}_r^{jk} (d_c^j + d_c^k)} \right]^{-1}, \quad (2.53)$$

where δ_r^{jk} and \bar{c}_r^{jk} are the mean square root of mean distance and velocity of particles, respectively.

$$\delta_r^{jk} = \sqrt{\delta_a^{j2} + \delta_a^{k2}}, \quad (2.54)$$

$$\bar{c}_r^{jk} = \sqrt{c^j2 + c^k2}. \quad (2.55)$$

Coagulation redistributes the total number of agglomerates and primary particles as well as hydrogen atoms among the sections. The partial coagulation source terms for N_{agg}^i , N_{pri}^i and H_{tot}^i can be calculated as:

$$I_{N_{agg}}^i = \sum_{k=1}^{n_{sec}} \sum_{j=k}^{n_{sec}} \left(1 - \frac{\delta_{jk}}{2}\right) \eta_{ijk} \beta^{jk} N_{agg}^j N_{agg}^k - N_{agg}^i \sum_{k=1}^{n_{sec}} \beta^{im} N_{agg}^m. \quad (2.56)$$

$$I_{N_{pri}}^i = \sum_{k=1}^{n_{sec}} \sum_{j=k}^{n_{sec}} \left(1 - \frac{\delta_{jk}}{2}\right) \eta_{p,ijk} \eta_{ijk} \beta^{jk} N_{agg}^j N_{agg}^k - N_{pri}^i \sum_{k=1}^{n_{sec}} \beta^{im} N_{agg}^m. \quad (2.57)$$

$$I_{H_{tot}}^i = \sum_{k=1}^{n_{sec}} \sum_{j=k}^{n_{sec}} \left(1 - \frac{\delta_{jk}}{2}\right) \eta_{h,ijk} \eta_{ijk} \beta^{jk} N_{agg}^j N_{agg}^k - H_{tot}^i \sum_{k=1}^{n_{sec}} \beta^{im} N_{agg}^m. \quad (2.58)$$

where δ_{jk} is the Kronecker delta defined as:

$$\delta_{jk} = \begin{cases} 1, & \text{if } j = k \\ 0, & \text{if } j \neq k \end{cases} \quad (2.59)$$

In Equation(2.56), η_{ijk} assigns newly formed agglomerates to the two consecutive section in order to conserves mass during coagulation [59].

$$\eta_{ijk} = \begin{cases} \frac{C_{agg}^{i+1} - C_{agg}^{jk}}{C_{agg}^{i+1} + C_{agg}^i}, & \text{if } C_{agg}^i \leq C_{agg}^{jk} < C_{agg}^{i+1} \\ \frac{C_{agg}^i - C_{agg}^{jk}}{C_{agg}^i + C_{agg}^{i-1}}, & \text{if } C_{agg}^{i-1} \leq C_{agg}^{jk} < C_{agg}^i \\ 0 & \text{else} \end{cases} \quad (2.60)$$

where $C_{agg}^{jk} = C_{agg}^j + C_{agg}^k$. Similarly, $\eta_{p,ijk}$ in Equation (2.57) and $\eta_{h,ijk}$ in Equation (2.58) adjust the number primary particles and hydrogen atoms added to consecutive sections based on their mass.

$$\eta_{p,ijk} = \frac{C_{agg}^i}{C_{agg}^{jk}} (n_p^j + n_p^k), \quad (2.61)$$

$$\eta_{h,ijk} = \frac{C_{agg}^i}{C_{agg}^{jk}} (H_{agg}^j + H_{agg}^k), \quad (2.62)$$

2.4.5.2 Source terms

The source terms are split into four part showing the contribution of different soot formation and evolution factors. The effect of surface growth and PAH adsorption are combined because they are similar mass gaining mechanisms.

$$S_{N_{agg}} = (S_{N_{agg}})_{inc} + (S_{N_{agg}})_{gr,ads} + (S_{N_{agg}})_{ox} + (S_{N_{agg}})_{coag}, \quad (2.63)$$

$$S_{N_{pri}} = (S_{N_{pri}})_{inc} + (S_{N_{pri}})_{gr,ads} + (S_{N_{pri}})_{ox} + (S_{N_{pri}})_{coag}, \quad (2.64)$$

$$S_{H_{tot}} = (S_{H_{tot}})_{inc} + (S_{H_{tot}})_{gr,ads} + (S_{H_{tot}})_{ox} + (S_{H_{tot}})_{coag}. \quad (2.65)$$

Inception introduces equal number of agglomerates and primary particles as well as hydrogen to the first section.

$$(S_{N_{agg}})_{inc} = \frac{1}{Av} \frac{I_{N,inc}}{C_{agg}^i}, \quad i = 1. \quad (2.66)$$

$$(S_{N_{pri}})_{inc} = \frac{1}{Av} \frac{I_{N,inc}}{C_{agg}^i}, \quad i = 1. \quad (2.67)$$

$$(S_{H_{tot}})_{inc} = I_{H,inc}, \quad i = 1. \quad (2.68)$$

Surface growth and PAH adsorption increase the (carbon) mass and hydrogen content of agglomerates, and transfer them to upper sections. The removal rate of agglomerates (N_{agg}^i) from the origin section due to surface growth and PAH adsorption must be equal to the addition rate of agglomerates to the target section to conserve the mass, and it is calculated by dividing the mass growth rate by the difference of the mass of the adjacent sections.

$$(S_{N_{agg}})_{gr,ads} = \frac{1}{Av} \begin{cases} -\frac{I_{C_{tot},gr}^i + I_{C_{tot},ads}^i}{C_{agg}^{i+1} - C_{agg}^i} & \text{if } i = 1 \\ \frac{I_{C_{tot},gr}^{i-1} + I_{C_{tot},ads}^{i-1}}{C_{agg}^i - C_{agg}^{i-1}} - \frac{I_{C_{tot},gr}^i + I_{C_{tot},ads}^i}{C_{agg}^{i+1} - C_{agg}^i} & \text{if } 1 < i < n_{sec} \\ \frac{I_{C_{tot},gr}^{i-1} + I_{C_{tot},ads}^{i-1}}{C_{agg}^i - C_{agg}^{i-1}} & \text{if } i = n_{sec} \end{cases} \quad (2.69)$$

As agglomerates migrate up/down through sections, they carry the number of primary particles as well as hydrogen atoms, so the transfer rate of agglomerates is multiplied by n_p^i and H_{agg}^i , respectively.

$$(S_{N_{pri}})_{gr,ads} = \frac{1}{Av} \begin{cases} -\frac{I_{C_{tot},gr}^i + I_{C_{tot},ads}^i}{C_{agg}^{i+1} - C_{agg}^i} & \text{if } i = 1 \\ \frac{I_{C_{tot},gr}^{i-1} + I_{C_{tot},ads}^{i-1}}{C_{agg}^i - C_{agg}^{i-1}} n_p^{i-1} - \frac{I_{C_{tot},gr}^i + I_{C_{tot},ads}^i}{C_{agg}^{i+1} - C_{agg}^i} n_p^i & \text{if } 1 < i < n_{sec} \\ \frac{I_{C_{tot},gr}^{i-1} + I_{C_{tot},ads}^{i-1}}{C_{agg}^i - C_{agg}^{i-1}} n_p^{i-1} & \text{if } i = n_{sec} \end{cases} \quad (2.70)$$

$$(S_{H_{tot}})_{gr,ads} = \frac{1}{Av} \begin{cases} -\frac{I_{C_{tot},gr}^i + I_{C_{tot},ads}^i}{C_{agg}^{i+1} - C_{agg}^i} H_{agg}^i + I_{H_{tot},gr}^i + I_{H_{tot},ads}^i & \text{if } i = 1 \\ \frac{I_{C_{tot},gr}^{i-1} + I_{C_{tot},ads}^{i-1}}{C_{agg}^i - C_{agg}^{i-1}} H_{agg}^{i-1} - \frac{I_{C_{tot},gr}^i + I_{C_{tot},ads}^i}{C_{agg}^{i+1} - C_{agg}^i} H_{agg}^i + I_{H_{tot},gr}^i + I_{H_{tot},ads}^i & \text{if } 1 < i < n_{sec} \\ \frac{I_{C_{tot},gr}^{i-1} + I_{C_{tot},ads}^{i-1}}{C_{agg}^i - C_{agg}^{i-1}} H_{agg}^{i-1} + I_{H_{tot},gr}^i + I_{H_{tot},ads}^i & \text{if } i = n_{sec} \end{cases} \quad (2.71)$$

Similarly, the agglomerates lose (carbon) mass by oxidation, and descend to the lower sections carrying primary particle and hydrogen.

$$(S_{N_{agg}})_{ox} = \frac{1}{Av} \begin{cases} \frac{I_{C_{tot},ox}^{i+1}}{C_{agg}^{i+1} - C_{agg}^i} - \frac{I_{C_{tot},ox}^i}{C_{agg}^i} & \text{if } i = 1 \\ \frac{I_{C_{tot},ox}^{i+1}}{C_{agg}^{i+1} - C_{agg}^i} - \frac{I_{C_{tot},ox}^i}{C_{agg}^i - C_{agg}^{i-1}} & \text{if } 1 < i < n_{sec} \\ -\frac{I_{C_{tot},ox}^i}{C_{agg}^i - C_{agg}^{i-1}} & \text{if } i = n_{sec} \end{cases} \quad (2.72)$$

$$(S_{N_{pri}})_{ox} = \frac{1}{Av} \begin{cases} \frac{I_{C_{tot},ox}^{i+1}}{C_{agg}^{i+1} - C_{agg}^i} n_p^{i+1} - \frac{I_{C_{tot},ox}^i}{C_{agg}^i} & \text{if } i = 1 \\ \frac{I_{C_{tot},ox}^{i+1}}{C_{agg}^{i+1} - C_{agg}^i} n_p^{i+1} - \frac{I_{C_{tot},ox}^i}{C_{agg}^i - C_{agg}^{i-1}} n_p^i & \text{if } 1 < i < n_{sec} \\ - \frac{I_{C_{tot},ox}^i}{C_{agg}^i - C_{agg}^{i-1}} n_p^i & \text{if } i = n_{sec} \end{cases} \quad (2.73)$$

$$(S_{H_{tot}})_{ox} = \frac{1}{Av} \begin{cases} \frac{I_{C_{tot},ox}^{i+1}}{C_{agg}^{i+1} - C_{agg}^i} H_{agg}^{i+1} - \frac{I_{C_{tot},ox}^i}{C_{agg}^i} H_{agg}^i + I_{H_{tot},ox}^i & \text{if } i = 1 \\ \frac{I_{C_{tot},ox}^{i+1}}{C_{agg}^{i+1} - C_{agg}^i} H_{agg}^{i+1} - \frac{I_{C_{tot},ox}^i}{C_{agg}^i - C_{agg}^{i-1}} H_{agg}^i + I_{H_{tot},ox}^i & \text{if } 1 < i < n_{sec} \\ - \frac{I_{C_{tot},ox}^i}{C_{agg}^i - C_{agg}^{i-1}} H_{agg}^i + I_{H_{tot},ox}^i & \text{if } i = n_{sec} \end{cases} \quad (2.74)$$

2.5 Surface reactions model

The heterogeneous surface reactions are described by hydrogen-abstraction-acetylene-addition (HACA) mechanism [30, 45]. The soot growth in HACA scheme is based on a sequential process similar to PAH growth. The hydrogenated arm-chair sites ($C_{soot} - H$) on the edge of aromatic rings are dehydrogenated (C_{soot}°) that can form bond with C_2H_2 adding an additional aromatic ring with hydrogenated site. These sites can also be attacked by O_2 or OH . The elementary reactions that describe this sequential process are listed in Table 2.1 The rate of mass growth by HACA is obtained from reaction of C_2H_2 with dehydrogenated sites as:

$$\omega_{gr}^i = \alpha^i k_{f4} [C_2H_2] [C_{soot}^\circ]. \quad (2.75)$$

where k_{f4} denotes the forward rate of 4th reaction in Table 2.1, and $[C_{soot}^\circ]$ is obtained by multiplying the surface density of dehydrogenated sites, χ_{soot}° with total surface area of soot (per unit of mass of gas mixture) as:

$$[C_{soot}^\circ] = \frac{\rho}{Av} A_{tot}^i \cdot \chi_{soot}^\circ. \quad (2.76)$$

χ_{soot}° is calculated by assuming the steady-state for $[C_{soot}^\circ]$ in the system of reactions in Table 2.1:

$$\chi_{soot}^\circ = \frac{k_{f1}[H] + k_{f2}[OH]}{k_{r1}[H_2] + k_{r2}[H_2O] + k_{f3}[H] + k_{f4}[C_2H_2] + k_{f5}[O_2] + k_{f1}[H] + k_{f2}[OH]} \chi_{sootCH}, \quad (2.77)$$

where χ_{sootCH} is the surface density of hydrogenated sites estimated based on the assumption that soot surface is covered with stacks of benzene rings [45]. Considering the stack spacing of 3.15Å and 2 C-H bonds per benzene ring length, the surface density of hydrogenated sites, χ_{soot-H} , is calculated to be $0.23 \text{ site}/\text{\AA}^2 = 2.3 \times 10^{19} \text{ site}/\text{m}^2$, which give the maximum theoretical limit of the reaction sites.

In Equation (2.75), α is the surface reactivity factor between 0 and 1 that represents the decline of reaction sites from the theoretical limit due to particle aging, growth and maturity [91, 92], and it has been observed to depend on temperature time history [93, 47]. The value of α has been described using constant target-specific values as well as empirical equations based on particle size and flame temperature. Blanquart and Pitsch [72] related α to the number of surface hydrogen atoms on the soot particles. A detailed review of these can be found in the chapter 4 of [94]. Here, the empirical

Table 2.1: Rate coefficients for the various surface reactions in Arrhenius form $k = AT^n \cdot e^{-E/RT}$

No.	Reaction		A $\left[\frac{\text{m}^3}{\text{mol}\cdot\text{s}}\right]$	n	$\frac{E}{R}[\text{K}]$
(R 2.1)	$\text{C}_{\text{soot-H}} + \text{H} \rightleftharpoons \text{C}_{\text{soot}^\circ} + \text{H}_2$	f	4.17×10^7	0	6542.52
		r	3.9×10^6	0	5535.98
(R 2.2)	$\text{C}_{\text{soot-H}} + \text{OH} \rightleftharpoons \text{C}_{\text{soot}^\circ} + \text{H}_2\text{O}$	f	10^4	0.734	719.68
		r	3.68×10^2	1.139	8605.94
(R 2.3)	$\text{C}_{\text{soot}^\circ} + \text{H} \longrightarrow \text{C}_{\text{soot}} + \text{H}_2\text{O}$	f	10^4	0.734	719.68
(R 2.4)	$\text{C}_{\text{soot}^\circ} + \text{C}_2\text{H}_2 \longrightarrow \text{C}_{\text{soot-H}}$	f	80	1.56	1912.43
(R 2.5)	$\text{C}_{\text{soot}^\circ} + \text{O}_2 \longrightarrow 2 \text{CO}$	f	2.2×10^6	0	3774.53
(R 2.6)	$\text{C}_{\text{soot-H}} + \text{OH} \longrightarrow \text{CO} + \frac{1}{2} \text{H}_2$	f	1.3×10^7	0	0

equations proposed by Appel et al. [45] is used to calculate α :

$$\alpha^i = \tanh \left(\frac{12.56 - 0.00563 \cdot T}{\log_{10} \left(\frac{\rho_{\text{soot}} \cdot A_v}{W_{\text{carbon}}} \frac{\pi}{6} d_p^3 \right)} - 1.38 + 0.00068 \cdot T \right). \quad (2.78)$$

The contribution of HACA to growth source terms can be computed from HACA rate considering the number of carbon atoms in C_2H_2 and number of arm-chair and zig-zag hydrogenated sites on soot particle [31] using

$$I_{C_{\text{tot}},gr}^i = 2\omega_{gr}^i / \rho, \quad (2.79)$$

$$I_{H_{\text{tot}},gr}^i = 0.25\omega_{gr}^i / \rho. \quad (2.80)$$

The rate change of C_2H_2 concentration due to mass growth is written as:

$$\left(\frac{d[\text{C}_2\text{H}_2]}{dt} \right)_{gr} = - \sum_{i=1}^{n_{\text{sec}}} \omega_{gr}^i. \quad (2.81)$$

The rate of release of H radicals into the gas mixture due to surface growth is:

$$\left(\frac{d[\text{H}]}{dt} \right)_{gr} = 1.75 \sum_{i=1}^{n_{\text{sec}}} \omega_{gr}^i. \quad (2.82)$$

The carbons on the surface of soot are oxidized via reaction with O_2 and OH which decreases total carbon of soot and releases CO and H_2 to gas mixture. The oxidation process is described by HACA mechanism. O_2 and OH oxidation rates are calculated as

$$\omega_{ox,O_2}^i = \alpha^i k_{f5} [\text{O}_2] [C_{\text{soot}^\circ}^i], \quad (2.83)$$

$$\omega_{ox,OH}^i = \alpha^i k_{f6} [\text{OH}] N_{agg}^i \rho. \quad (2.84)$$

The oxidation source term is calculated considering the number of carbon atoms removed from soot through each oxidation pathway by

$$I_{C_{\text{tot}},ox}^i = -(2\omega_{ox,O_2}^i + \omega_{ox,OH}^i) / \rho, \quad (2.85)$$

We assume that oxidation does not change the number of surface hydrogen atoms. The rate change of concentration of CO , H and OH by oxidation is calculates as:

$$\left(\frac{d[\text{CO}]}{dt}\right)_{ox} = \sum_{i=1}^{n_{sec}} \omega_{ox,O_2}^i. \quad (2.86)$$

$$\left(\frac{d[\text{O}_2]}{dt}\right)_{ox} = - \sum_{i=1}^{n_{sec}} \omega_{ox,O_2}^i. \quad (2.87)$$

$$\left(\frac{d[\text{OH}]}{dt}\right)_{ox} = - \sum_{i=1}^{n_{sec}} \omega_{ox,OH}^i. \quad (2.88)$$

$$\left(\frac{d[\text{H}_2]}{dt}\right)_{ox} = \frac{1}{2} \sum_{i=1}^{n_{sec}} \omega_{ox,OH}^i. \quad (2.89)$$

2.6 PAH growth models

Here, four different PAH growth models are used to describe the conversion of PAHs to incipient particles and their adsorption on existing agglomerates. All models are collision-based consisting of different pathways with single- or multi-step reactions. The collision frequency of gaseous species including PAH molecules and polymers depend on their mass and diameter, and it is obtained as:

$$\beta_{dim_{jk}} = 2.2 \cdot Av \cdot d_r^2 \sqrt{\frac{8\pi k_B T}{m_r}} \quad (2.90)$$

where d_r and m_r are reduced diameter and mass for two PAH molecule, respectively.

$$d_r = 2 \frac{d_{PAH_k} \cdot d_{PAH_j}}{d_{PAH_k} + d_{PAH_j}} \quad (2.91)$$

$$m_r = \frac{m_{PAH_k} \cdot m_{PAH_j}}{m_{PAH_k} + m_{PAH_j}} \quad (2.92)$$

The mass of each PAH molecule is obtained from its molecular weight as:

$$m_{PAH_j} = \frac{W_{PAH_j}}{Av} \quad (2.93)$$

The diameter of PAH is calculated from the mass and the density.

$$d_{PAH_j} = \left(\frac{6 \cdot m_{PAH_j}}{\pi \cdot \rho_{PAH_j}} \right)^{1/3} \quad (2.94)$$

The density of a PAH molecule is estimated using the relation proposed by Johansson et al. [95].

$$\rho_{PAH_j} = 171943.5197 \frac{W_C n_{C,PAH_j} + W_H n_{H,PAH_j}}{n_{C,PAH_j} + n_{H,PAH_j}} \quad (2.95)$$

The collision frequency of PAH_j and soot agglomerates in each section can be determined for the entire regime by harmonic mean of the collision frequency in the free molecular and continuum regimes as:

$$\beta_{ads_j}^i = \frac{\beta_{fm,ads}^i \cdot \beta_{cont,ads}^i}{\beta_{fm,ads}^i + \beta_{cont,ads}^i} \quad (2.96)$$

$$\beta_{fm,ads_j}^i = 2.2 \sqrt{\frac{\pi k_B T}{2} \left(\frac{1}{m_{agg}^i} + \frac{1}{m_{PAH_j}} \right)} (d_g^i + d_{PAH_j})^2 \quad (2.97)$$

$$\beta_{cont,ads_j}^i = \frac{2k_B T}{3\mu} \left[\frac{C^i(d_m)}{d_g^i} + \frac{C^i(d_{PAH_j})}{d_{PAH_j}} \right] (d_g + d_{PAH_j}) \quad (2.98)$$

2.6.1 Irreversible Dimerization

The irreversible dimerization is based on the collision-based clustering/polymerization PAHs that form dimers, trimers, and tetramers until the polymer mass reaches a threshold that can be considered a solid particle. For practical purposes, dimer is usually considered as a incipient particle that grows by surface growth and coagulation. A single-step irreversible collision of two similar PAHs forms a new dimer as:



Similarly, the adsorption of each PAH molecule on soot particles is described by the irreversible collision of soot and PAH_j as:



The forward rate of dimerization, k_{f, dim_j} and adsorption, k_{f, ads_j} in Reactions (R 2.7) and (R 2.8) are calculated from Equations (2.90) and (2.96), respectively.

$$k_{f, \text{dim}_j} = \gamma_{\text{inc}} \cdot \beta_{jk, \text{PAH}} \cdot Av, \quad (2.99)$$

$$k_{f, \text{ads}}^i = \gamma_{\text{ads}} \cdot \beta_{jk, \text{ads}}^i \cdot Av, \quad (2.100)$$

where γ_{inc} and γ_{ads} are collision efficiencies for dimerization and adsorption, respectively. Their value vary in $[10^{-7}, 1]$ range, and usually selected to match the predicted soot mass with the experimental data. Here, $\gamma_{\text{inc}} = 10^{-4}$ and $\gamma_{\text{ads}} = 10^{-3}$. The rate of dimerization and adsorption from PAH_j are calculated accordingly as:

$$w_{\text{dim}_j} = k_{f, \text{dim}_j} [\text{PAH}_j] [\text{PAH}_j] \quad (2.101)$$

The partial source terms for inception are calculated as:

$$I_{N, \text{inc}} = \frac{1}{\rho} \sum_{j=1}^{n_{\text{PAH}}} w_{\text{dim}_j} 2n_{\text{PAH}_j, C} \quad (2.102)$$

$$I_{C_{\text{tot}}, \text{inc}} = \frac{1}{\rho} \sum_{j=1}^{n_{\text{PAH}}} w_{\text{dim}_j} 2n_{\text{PAH}_j, C} \quad (2.103)$$

$$I_{H_{\text{tot}}, \text{inc}} = \frac{1}{\rho} \sum_{j=1}^{n_{\text{PAH}}} w_{\text{dim}_j} 2n_{\text{PAH}_j, H} \quad (2.104)$$

The rate of PAH adsorption for each section is obtained as:

$$w_{\text{ads}_j}^i = k_{f, \text{ads}_j}^i [\text{Soot}] [\text{PAH}_j] \quad (2.105)$$

The contribution of PAH adsorption to the source terms are expressed as:

$$I_{C_{\text{tot}}, \text{ads}}^i = \frac{1}{\rho} \sum_{j=1}^{n_{\text{PAH}}} w_{\text{ads}_j}^i n_{\text{PAH}, C} \quad (2.106)$$

$$I_{H_{\text{tot}}, \text{ads}}^i = \frac{1}{\rho} \sum_{j=1}^{n_{\text{PAH}}} w_{\text{ads}_j}^i (n_{\text{PAH}, H} - 2) \quad (2.107)$$

Each PAH molecule loses one H atom becoming a radical that forms bonds with a dehydrogenated site on soot surface, so two H atoms are released during the process that is taken into account in Equation (2.107).

The formation of a dimer consumes two PAH molecules, and during adsorption one PAH molecule is removed from the gas mixture, so the total rate of PAH_i removal by the irreversible dimerization is obtained as:

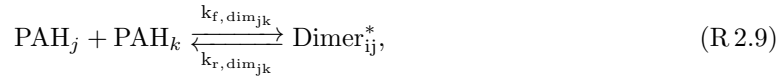
$$\left(\frac{d[\text{PAH}_j]}{dt}\right)_{inc} = -2w_{dim_j} - \sum_{i=1}^{n_{sec}} w_{ads_j}^i. \quad (2.108)$$

During the adsorption process one H_2 is released to the gas mixture.

$$\left(\frac{d[\text{H}_2]}{dt}\right)_{inc} = \sum_{i=1}^{n_{sec}} w_{ads_j}^i. \quad (2.109)$$

2.6.2 Reactive Dimerization

The design of this approach is similar to irreversible dimerization with two main differences: The first step of dimerization and adsorption is reversible forming physically bonded dimers followed by a irreversible carbonization that leads to chemical bond formation in dimers [42]. This approach allows formation of homo- and heterodimers. The dimerization of PAH_j and PAH_k is described as:



where Dimer_{jk}^* and Dimer_{jk} physically and chemically bonded dimers, respectively, from PAH_j and PAH_k . The forward rate of physical dimerization, $k_{f,dim_{jk}}$ is calculated from Equation (2.90) as:

$$k_{f,dim_{jk}} = p'' \cdot \beta_{jk,PAH} \cdot Av, \quad (2.110)$$

where $p'' = 0.1$ accounts for the probability of PAH-PAH collisions in “FACE” configuration that results in successful van der Waals formation [96]. The reverse rate of physical dimerization, $k_{r,dim_{jk}}$ is obtained from the dimerization equilibrium constant [38] as:

$$\log_{10} K_{eq} = a \frac{\epsilon_{jk}}{RT} + b, \quad (2.111)$$

$$k_{r,dim_{jk}} = k_{f,dim_{jk}} 10^{-b} e^{-a\epsilon_{jk} \ln(10)/(RT)}, \quad (2.112)$$

$$\epsilon_{jk} = cW_{jk} - d, \quad (2.113)$$

$$W_{jk} = \frac{W_j \cdot W_k}{W_j + W_k}, \quad (2.114)$$

where $a = 0.115$ (obtained from pyrere dimerization data [33]) and $b=1.8$ [42], $c=933420$ J/kg, and $d=34053$ J/mol [42].

The rate of chemical bond formation, k_{REAC} is defined in the Arrhenius form [34] as

$$k_{c,dim} = 5 \times 10^6 \cdot e^{(-96232/RT)}. \quad (2.115)$$

Assuming a steady state condition for the physical dimers, $\partial[\text{Dimer}_{jk}^*]/\partial t = 0$, the rate of formation of the chemically-bonded dimer can be obtained as

$$\omega_{dim_{jk}} = k_{reac} \frac{k_{f,dim_{jk}} [\text{PAH}_j] [\text{PAH}_k]}{k_{r,dim_{jk}} + k_{c,dim}}. \quad (2.116)$$

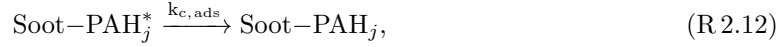
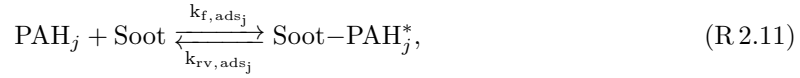
The contribution of dimer formation to partial source terms is expressed by looping over all combinations of PAHs as:

$$I_{N,inc} = \frac{1}{\rho} \sum_{j=1}^{n_{PAH}} \sum_{k=j}^{n_{PAH}} \omega_{dim_{kj}} (n_{PAH_j,C} + n_{PAH_k,C}), \quad (2.117)$$

$$I_{C_{tot},inc} = \frac{1}{\rho} \sum_{j=1}^{n_{PAH}} \sum_{k=j}^{n_{PAH}} \omega_{dim_{kj}} (n_{PAH_j,C} + n_{PAH_k,C}), \quad (2.118)$$

$$I_{H_{tot},inc} = \frac{1}{\rho} \sum_{j=1}^{n_{PAH}} \sum_{k=j}^{n_{PAH}} \omega_{dim_{kj}} (n_{PAH_j,H} + n_{PAH_k,H}), \quad (2.119)$$

Similarly, PAH adsorption is described by a two-step process where the collision of PAH_j with soot agglomerates leads to physically bonded Soot – PAH* that is carbonized and forms chemically-bonded Soot – PAH added to soot surface.



The forward rate of PAH-soot collision is calculated from Equation (2.96), and the reverse rate is determined same as inception (Equation(2.112)).

$$k_{f,ads}^i = \beta_{jk,ads}^i \cdot Av, \quad (2.120)$$

$$k_{r,ads}^i = k_{f,ads}^i \cdot 10^{-b} e^{-a\epsilon_{soot,j} \ln(10)/(RT)}, \quad (2.121)$$

$$\epsilon_{soot,j} = cW_{soot,j} - d, \quad (2.122)$$

a, b, c, d values are the same as inception. Computing $\epsilon_{soot,j}$ also requires "equivalent soot molecular weight", W_{soot} for section i, which is estimated from carbon mass of each agglomerate as:

$$MW_{soot}^i = \frac{C_{tot}^i W_{carbon}}{N_{agg}^i} \quad (2.123)$$

The rate constant of carbonization of Soot – PAH_j* is defined as in the Arrhenius form similar to inception (Equation (??)). The prefactor is adjusted based on matching the numerical PSD [34] with measurements in the ethylene pyrolysis in flow reactor [97].

$$k_{c,dim} = 2 \times 10^{10} \cdot e^{(-96232/RT)}. \quad (2.124)$$

The total adsorption rate can be calculated assuming a steady-state concentration for physically adsorbed PAH on soot, $\partial[Soot - PAH^*]/\partial t = 0$, similar to inception rate (Equation (??)) as

$$\omega_{ads_j}^i = k_{c,ads} \frac{k_{f,ads_j} [Soot][PAH_j]}{k_{r,ads_j} + k_{c,ads_j}}, \quad (2.125)$$

The contribution of PAH adsorption rate to partial source terms can be expressed as:

$$I_{C_{tot},ads}^i = \frac{1}{\rho} \sum_{i=1}^{n_{PAH}} \omega_{ads_j}^i n_{C,PAH_j}, \quad (2.126)$$

$$I_{H_{tot},ads}^i = \frac{1}{\rho} \sum_{i=1}^{n_{PAH}} \omega_{ads_j}^i (n_{H,PAH_j} - 2). \quad (2.127)$$

The rate of removal of PAH from gas mixture due to adsorption is given as

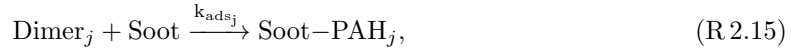
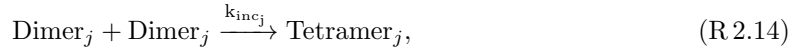
$$\left(\frac{d[\text{PAH}_j]}{dt}\right)_{inc} = - \sum_{k=1}^{n_{PAH}} w_{dim_{jk}} - \sum_{i=1}^{n_{sec}} w_{ads_j}^i. \quad (2.128)$$

During the adsorption process one H_2 is released to the gas mixture.

$$\left(\frac{d[\text{H}_2]}{dt}\right)_{inc} = \sum_{i=1}^{n_{sec}} w_{ads_j}^i. \quad (2.129)$$

2.6.3 Dimer Coalescence

Dimer coalescence model is a multi-step irreversible model proposed by Blanquart and Pitsch [72] where self-collision of PAH molecules form dimers that are intermediate state between gaseous PAH molecules and solid soot particles. The self-coalescence of dimers forms incipient soot particles. Alternatively, dimers can adsorb on the surface of existing soot particles and contribute to their surface growth. The equations are based on implementation of Dimer Coalescence by Sun et al. [98] for a sectional model.



where the rate constant of dimerization, k_{dim_j} and inception k_{inc_j} are calculated from collision rate of PAHs in Equation (2.96).

$$k_{dim_j} = \gamma_{dim_j} \cdot \beta_{jj,PAH} \cdot Av, \quad (2.130)$$

$$k_{inc_j} = \beta_{jj,dimer} \cdot Av, \quad (2.131)$$

where γ_{dim_j} is the dimerization efficiency that is assumed to scale with fourth power of PAH molecular weight [31] as:

$$\gamma_{dim_j} = C_{N,j} \cdot W_{PAH_j}^4, \quad (2.132)$$

Blanquart and Pitsch [72] estimated the constant $C_{N,j}$ by comparing the profiles of several PAH species with experimental measurements in a single premixed benzene flame [99], and provided a efficiency values for various PAHs that are listed in Table 2.2. The rate dimer of coalescence is expressed as:

$$w_{dim_j} = k_{inc_j} [\text{Dimer}_j] [\text{Dimer}_j] \quad (2.133)$$

Similarly, the rate of adsorption of dimers on soot particles is obtained as:

$$w_{ads_j}^i = k_{ads_j}^i [\text{Soot}]^i [\text{Dimer}_j] \quad (2.134)$$

Assuming fast dimer consumption leads to the steady-state concentration of the dimer that can be determined by solving a quadratic equation as:

$$a_{inc_j} [\text{dimer}]^2 + b_{ads_j} [\text{dimer}] = \omega_{dim,j} \quad (2.135)$$

$$[\text{Dimer}_j] = \begin{cases} \frac{-b_{ads_j} + \sqrt{\Delta_j}}{2a_{inc_j}}, & \text{if } \Delta_j \geq 0 \\ 0 & \text{if } \Delta_j < 0 \end{cases} \quad (2.136)$$

$$\Delta_j = b_{ads_j}^2 - 4a_{inc_j} \omega_{dim,j} \quad (2.137)$$

Table 2.2: The dimerization efficiency, γ_{dim_j} , for different PAH in dimer coalescence model[31]

Species name	Chemical formula	W [kg/mol]	γ_{dim_j}
Naphthalene	C_{10}H_8	0.128	0.002
Acenaphthylene	C_{12}H_8	0.152	0.004
Biphenyl	$\text{C}_{12}\text{H}_{10}$	0.154	0.0085
Phenathrene	$\text{C}_{14}\text{H}_{10}$	0.178	0.015
Acephenanthrylene	$\text{C}_{16}\text{H}_{10}$	0.202	0.025
Pyrene	$\text{C}_{16}\text{H}_{10}$	0.202	0.025
Fluoranthene	$\text{C}_{16}\text{H}_{10}$	0.202	0.025
Cyclopenta[cd]pyrene	$\text{C}_{18}\text{H}_{10}$	0.226	0.039

where $a_{\text{inc}_j} = k_{\text{inc}_j}$ and b_{ads_j} is calculated by summing the adsorption rate of dimer for all sections and dividing it by the dimer concentration.

$$b_{\text{ads}_j} = \sum_{i=1}^{n_{\text{sec}}} k_{\text{ads}_j}^i [\text{Soot}]^i \quad (2.138)$$

After determining the concentration of each dimer, the contribution of inception and PAH adsorption to source terms of tracked soot variables can be calculated similar to previous inception models.

$$I_{N,\text{inc}} = \frac{1}{\rho} \sum_{j=1}^{n_{\text{PAH}}} 4\omega_{\text{inc}_j} n_{\text{PAH}_j,C}, \quad (2.139)$$

$$I_{C_{\text{tot}},\text{inc}} = \frac{1}{\rho} \sum_{j=1}^{n_{\text{PAH}}} 4\omega_{\text{inc}_j} n_{\text{PAH}_j,C}, \quad (2.140)$$

$$I_{H_{\text{tot}},\text{inc}} = \frac{1}{\rho} \sum_{j=1}^{n_{\text{PAH}}} 4\omega_{\text{inc}_j} (n_{\text{PAH}_j,H} - 2), \quad (2.141)$$

$$I_{C_{\text{tot}},\text{ads}}^i = \frac{1}{\rho} \sum_{i=1}^{n_{\text{PAH}}} 2\omega_{\text{ads}_j}^i n_{C,\text{PAH}_j}, \quad (2.142)$$

$$I_{C_{\text{tot}},\text{ads}}^i = \frac{1}{\rho} \sum_{i=1}^{n_{\text{PAH}}} 2\omega_{\text{ads}_j}^i (n_{H,\text{PAH}_j} - 2). \quad (2.143)$$

The rate of removal of PAHs and release of H_2 due to inception and PAH adsorption is calculated as:

$$\left(\frac{d[\text{PAH}_j]}{dt} \right)_{\text{inc}} = -4 \sum_{k=1}^{n_{\text{PAH}}} w_{\text{inc}_j} - 2 \sum_{i=1}^{n_{\text{sec}}} w_{\text{ads}_j}^i. \quad (2.144)$$

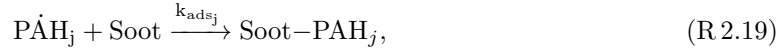
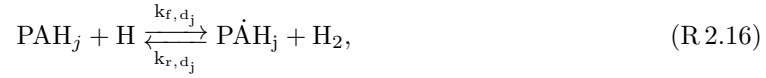
$$\left(\frac{d[\text{H}_2]}{dt} \right)_{\text{inc}} = 2 \sum_{i=1}^{n_{\text{sec}}} w_{\text{ads}_j}^i. \quad (2.145)$$

Table 2.3: Rate coefficients for the monomer de-/hydrogenation reaction of E-bridge formation in Arrhenius form $k = AT^n \cdot e^{-E/RT}$ [43]

Reaction		A $\left[\frac{\text{m}^3}{\text{mol} \cdot \text{s}} \right]$	n	$\frac{E}{R}$ [K]
(R 2.16)	f	$98 \times n_{C,PAH_j}$	1.8	7,563.519
	r	1.6×10^{-2}	2.63	2145.346
(R 2.17)	f	4.8658×10^7	0.13	0.0

2.6.4 E-Bridge Formation

The E-Bridge Formation was originally proposed by Frenklach and Mebel [43] to describe soot inception using a HACA-like scheme that starts with dehydrogenation of PAH monomers, often pyrene, the monomer radicals and continues with sequential addition of the radicals to PAHs that form dimers, trimers and larger polymers until the PAH structure reaches the mass threshold and the clustering process becomes irreversible. Here, a modified version of EBridge formation model is used where dimers are considered as incipient soot, and monomer radical are adsorbed on soot agglomerates. This PAH growth model is described using the following set of pathways:



The rate constants of Reactions (R 2.16)&(R 2.17) are listed in Table [?] while those of dimer production and adsorption are calculated based on Equations (2.90)&(2.96), respectively. For both steps, it is assumed the all collisions are successful i.e. 100% collision efficiency for radical-monomer and radical-soot.

$$k_{inc_j} = \beta_{jj,PAH} \cdot Av, \quad (2.146)$$

$$k_{ads_j}^i = \beta_{ads_j}^i \cdot Av, \quad (2.147)$$

The rate of dimer formation and adsorption is calculated as:

$$w_{dim_j} = k_{inc_j} [PAH_j] [P\dot{A}H_j] \quad (2.148)$$

$$w_{ads_j}^i = k_{ads_j}^i [\text{Soot}]^i [P\dot{A}H_j] \quad (2.149)$$

The calculations of rate of inception and PAH adsorption from PAH_j requires the concentration of corresponding monomer radical that can be determined by applying the steady-state assumption for $P\dot{A}H_j$.

$$\begin{aligned} \frac{d[P\dot{A}H_j]}{dt} = 0 \\ k_{f,d_j} [PAH_j] [H] - k_{r,d_j} [P\dot{A}H_j] [H_2] - k_{f,h_j} [P\dot{A}H_j] [H] - k_{inc_j} [P\dot{A}H_j]^2 \\ - \sum_{i=1}^{n_{sec}} k_{ads_j}^i [P\dot{A}H_j] [\text{Soot}]^i = 0 \end{aligned}$$

The above equations can be rearranged as a quadratic equation similar to the dimer coalescence.

$$a_{inc_j}[\dot{\text{PAH}}_j]^2 + b_{ads_j}[\dot{\text{PAH}}_j] + c_j = 0, \quad (2.150)$$

$$a_{inc_j} = k_{f,d_j} \quad (2.151)$$

$$b_{ads_j} = k_{r,d_j}[\text{H}_2] + k_{f,h_j}[\text{H}] + \sum_{i=1}^{n_{sec}} k_{ads_j}^i [\text{Soot}]^i \quad (2.152)$$

$$c_{inc_j} = k_{f,d_j}[\text{PAH}_j][\text{H}] \quad (2.153)$$

Finally, solving the quadratic equation for each PAH results in concentration of the radical using the following equation as:

$$[\dot{\text{PAH}}_j] = \begin{cases} \frac{-b_{ads_j} + \sqrt{\Delta_j}}{2a_{inc_j}}, & \text{if } \Delta_j \geq 0 \\ 0 & \text{if } \Delta_j < 0 \end{cases} \quad (2.154)$$

$$\Delta_j = b_{ads_j}^2 - 4a_{inc_j}c_j \quad (2.155)$$

The contribution of inception and adsorption to the partial source terms for E-Bridge formation can be written as:

$$I_{N,inc} = \frac{1}{\rho} \sum_{j=1}^{n_{PAH}} 2\omega_{inc_j} n_{PAH_j,C}, \quad (2.156)$$

$$I_{C_{tot},inc} = \frac{1}{\rho} \sum_{j=1}^{n_{PAH}} 2\omega_{inc_j} n_{PAH_j,C}, \quad (2.157)$$

$$I_{H_{tot},inc} = \frac{1}{\rho} \sum_{j=1}^{n_{PAH}} 2\omega_{inc_j} (n_{PAH_j,H} - 2), \quad (2.158)$$

$$I_{C_{tot},ads}^i = \frac{1}{\rho} \sum_{i=1}^{n_{PAH}} \omega_{ads_j}^i n_{C,PAH_j}, \quad (2.159)$$

$$I_{C_{tot},ads}^i = \frac{1}{\rho} \sum_{i=1}^{n_{PAH}} \omega_{ads_j}^i (n_{H,PAH_j} - 2). \quad (2.160)$$

The rate of removal of each PAH involved in soot inception and PAH adsorption and release of H_2 to the gas mixture can be expressed as:

$$\left(\frac{d[\text{PAH}_j]}{dt} \right)_{inc} = -2 \sum_{k=1}^{n_{PAH}} w_{inc_j} - \sum_{i=1}^{n_{sec}} w_{ads_j}^i. \quad (2.161)$$

$$\left(\frac{d[\text{H}_2]}{dt} \right)_{inc} = \sum_{i=1}^{n_{sec}} w_{ads_j}^i. \quad (2.162)$$

2.7 Gas scrubbing rates

The rate of production/destruction of species involved in soot formation must be taken into account to preserve the mass and energy balance in reactive system. In order to do that, the production rate of gaseous species calculated by Cantera must be corrected for the rate of release/consumption due to PAH growth and surface reaction models. PAHs participate in inception and PAH adsorption processes.

$$\left(\frac{d[\text{PAH}_j]}{dt}\right)_{tot} = \left(\frac{d[\text{PAH}_j]}{dt}\right)_{gas} + \left(\frac{d[\text{PAH}_j]}{dt}\right)_{inc} + \left(\frac{d[\text{PAH}_j]}{dt}\right)_{ads}. \quad (2.163)$$

H₂ is released to the gas mixture due to inception, PAH adsorption as well as oxidation.

$$\left(\frac{d[\text{H}_2]}{dt}\right)_{tot} = \left(\frac{d[\text{H}_2]}{dt}\right)_{gas} + \left(\frac{d[\text{H}_2]}{dt}\right)_{inc} + \left(\frac{d[\text{H}_2]}{dt}\right)_{ads} + \left(\frac{d[\text{H}_2]}{dt}\right)_{ox}. \quad (2.164)$$

Surface growth consumes C₂H₂ and adds H₂ to the gas mixture.

$$\left(\frac{d[\text{C}_2\text{H}_2]}{dt}\right)_{tot} = \left(\frac{d[\text{C}_2\text{H}_2]}{dt}\right)_{gas} + \left(\frac{d[\text{C}_2\text{H}_2]}{dt}\right)_{gr}. \quad (2.165)$$

$$\left(\frac{d[\text{H}]}{dt}\right)_{tot} = \left(\frac{d[\text{H}]}{dt}\right)_{gas} + \left(\frac{d[\text{H}]}{dt}\right)_{gr}. \quad (2.166)$$

Oxidation uses O₂ and OH to remove carbon from soot particles and generates H₂ and CO.

$$\left(\frac{d[\text{CO}]}{dt}\right)_{tot} = \left(\frac{d[\text{CO}]}{dt}\right)_{gas} + \left(\frac{d[\text{CO}]}{dt}\right)_{ox}. \quad (2.167)$$

$$\left(\frac{d[\text{O}_2]}{dt}\right)_{tot} = \left(\frac{d[\text{O}_2]}{dt}\right)_{gas} + \left(\frac{d[\text{O}_2]}{dt}\right)_{ox}. \quad (2.168)$$

$$\left(\frac{d[\text{OH}]}{dt}\right)_{tot} = \left(\frac{d[\text{OH}]}{dt}\right)_{gas} + \left(\frac{d[\text{OH}]}{dt}\right)_{ox}. \quad (2.169)$$

Chapter 3

Results

3.1 Validation

3.1.1 Collision Frequency

The collision frequency function determines the rate at which two particles collide resulting in the reduction of total number of particles and increase in their average size. In the absence of strong flow shear or external forces, Brownian motion is the main driving force for particle coagulation. As explained in Sections 2.4.4.1 & 2.4.5.1, omnisoot employs harmonic mean and Fuchs interpolations to calculate collision frequency of agglomerates from free-molecular to continuum regimes based on gas mean free path, and particle morphology.

The test case for validation of collision frequency is based on DEM simulation of 2000 monodisperse spherical particles with the density of 2200 kg/m^3 in a cubic cell with the constant temperature of 298 K and pressure of 1 atm [100]. Figure 3.1 depicts the collision frequency plotted against Knudsen number ($\text{Kn} = 2\lambda/d_m$) obtained by omnisoot using harmonic mean (red solid line) and Fuchs interpolation (green dashed line) and DEM results of Goudeli et al. [100]. The Fuchs interpretation perfectly matches DEM data over the free-molecular ($\text{Kn} < 10$) to the continuum ($\text{Kn} > 10$) range. However, harmonic mean slightly underpredicts the collision frequency in the transition regime ($0.1 \leq \text{Kn} \leq 10$) with relative errors less than 16%.

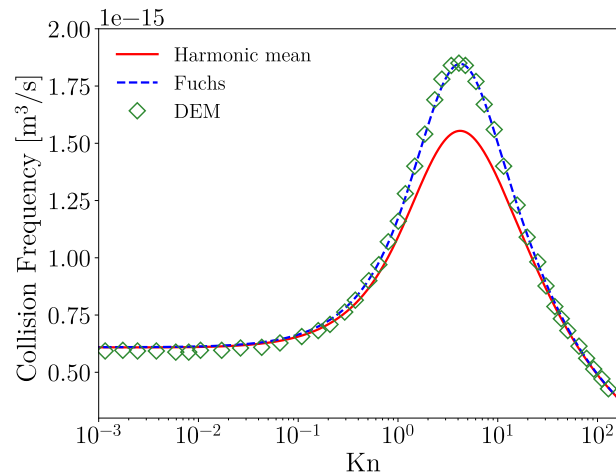


Figure 3.1: The comparison of collision frequency, β , obtained by omnisoot using harmonic mean (red solid line) and Fuchs interpolation (green dashed line) with DEM results (symbols) [100]

3.1.2 Coagulation

This test case was designed and conducted to validate the coagulation sub-unit of both particle dynamics models, MPBM and SPBM, by comparing the results of omnisooot with those of DEM [101]. The constant volume reactor was used for this test case, but it will be applicable to other reactors and flame models as long as the particle residence time matches with the values obtained by DEM. An adiabatic reactor with the volume of 1m^3 is initialized with 2.6261×10^{18} spherical particles that are 2 nm in diameter. The initial conditions are indicated in Table 3.1. The particles are allowed to coagulate in the free molecular regime and grow in size while inception, PAH adsorption and surface growth are disabled. Figure 3.3 demonstrates the number density of agglomerates (N_{agg}) and primary particles (N_{pri}), and mobility (d_m) and gyration (d_g) diameters of particle obtained by omnisooot that are in good agreement with DEM results. N_{pri} is conserved during coagulation resulting in identical flat lines for both particle dynamics models, but N_{agg} declines over time with the higher decay rate for SPBM because it accounts for the polydispersity of agglomerates that results in larger collision frequency compared to MPBM. Stronger collision rate leads to agglomerates with larger the mobility and gyrations diameters.

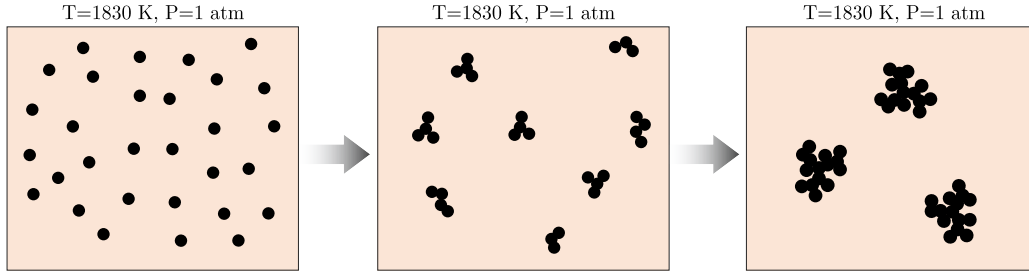


Figure 3.2: The schematic of agglomeration process in the coagulation test cases where initially spherical particle collide and form agglomerate

MPBM model does resolve PSD based on the assumption that at high concentrations particles reach their SPSPD, and their evolution can be described by tracking average properties. In contrast, SPBM tracks the number concentration of particles in fixed size sections that can be used to construct PSD and calculate mean and spread of size distribution of particle during coagulation. The left pane of Figure 3.4 shows the standard deviation of mobility diameter, σ_g in a close agreement with DEM results. Initially, σ_g is 1 indicating a monodisperse population at the beginning of the simulation, and it finally reaches 2.03 that is the signature standard deviation of the free molecular regime [102]. The right pane of Figure 3.4 demonstrates the evolution of non-dimensional PSD from $t=1$ ms to 677 ms. The PSD is shown in terms of the normalized concentration, $\Psi = \bar{v}n_{\text{agg}}(v, t)/N_{\text{agg,inf}}$ and dimensionless volume, $\eta = v/\bar{v}$, where $n_{\text{agg}}(v, t)$ is the size distribution function of agglomerate, v particle volume, \bar{v} mean particle volume, $N_{\text{agg,inf}}$ total number concentration of agglomerates. For short residence times, $t \approx 4$ ms, the PSD resembles a half bell curve because the majority of particles has sizes close to $d_0 = 2\text{nm}$ with the average volume close to the minimum volume, so particle with $\eta \approx 1$ has the largest concentration. As particles growth by coagulation, the PSD rapidly transitions to a full bell-curve ($t \geq 22\text{ms}$) and does not change for longer residence times, $t \geq 447\text{ms}$ marking the attainment of SPSPD. This confirms the ability of SPBM in omnisooot to capture SPSPD for soot agglomerates as a signature of Brownian-driven particle coagulation.

3.1.3 Constant Volume Reactor

The pyrolysis of 30% CH_4 diluted in N_2 with the initial temperature and pressure of 2455 K and 3.47 atm, respectively, was simulated using the constant volume reactor model in the residence time of 40 ms. The simulation was performed for 8 cases. The combination of available PAH growth and particle dynamics models leads to eight different cases that were simulated to ensure the conservation of mass and energy. Here, we focus on the total elemental balance of carbon and

Table 3.1: The simulations conditions of the coagulation test case [101]

Property	Value
Composition	CH ₄ :0.425, O ₂ :0.435, N ₂ :0.14
T	1830 K
P	1 atm
N_{agg}^1	$3.514 \times 10^{-5} \text{ mol/kg}$
N_{pri}^1	$3.514 \times 10^{-5} \text{ mol/kg}$
d_p^1	2 nm

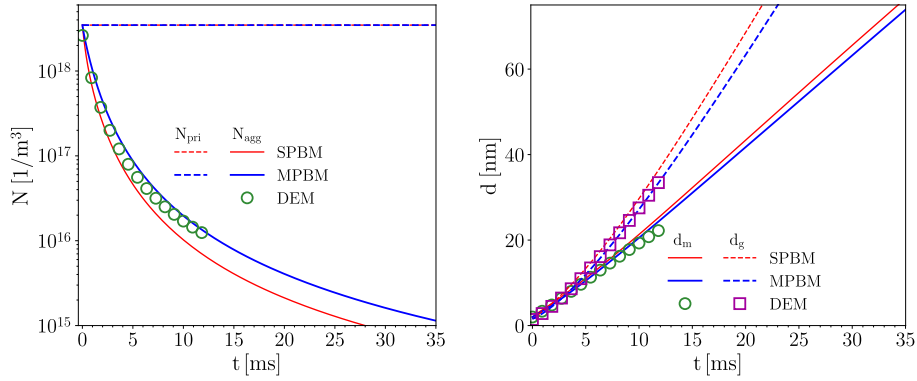


Figure 3.3: The total number concentration of agglomerates and primary particles (left pane), and mobility and gyration diameter (right pane) obtained with omnisooot using MPBM and SPBM that are in close agreement with the DEM results [101] indicating the validation of coagulation sub-model

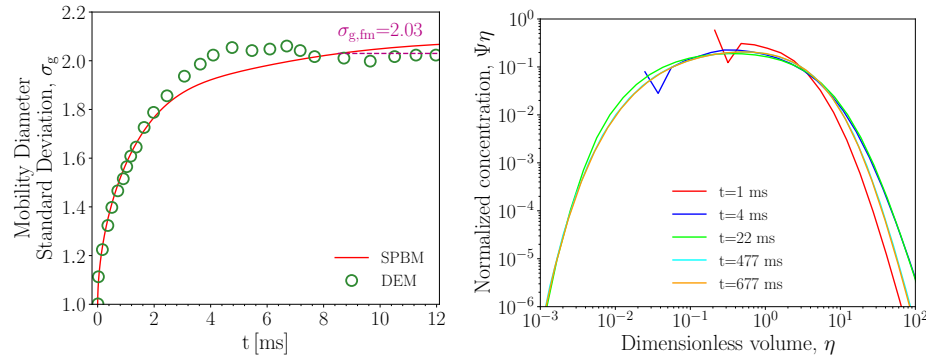


Figure 3.4: The standard deviation of mobility diameter, σ_g obtained with SPBM in close agreement with DEM results [101] (left pane) that reaches $\sigma_{g, \text{fm}} = 2.03$ characteristic of the free molecular regime [102]; the particle size distribution (normalized number concentration of agglomerates is plotted against non-dimensional volume in the right pane) at different residence times that overlaps after initial transient phase marking the attainment of self-preserving size distribution

hydrogen because they are involved in soot processes. Figure 3.5 demonstrates the relative error of total carbon, hydrogen and energy of system for different PAH growth and particle dynamics models in the constant volume that falls below 10^{-10} for all parameters confirming the validity of model in satisfying the mass and energy balance in the constant volume reactor using all models.

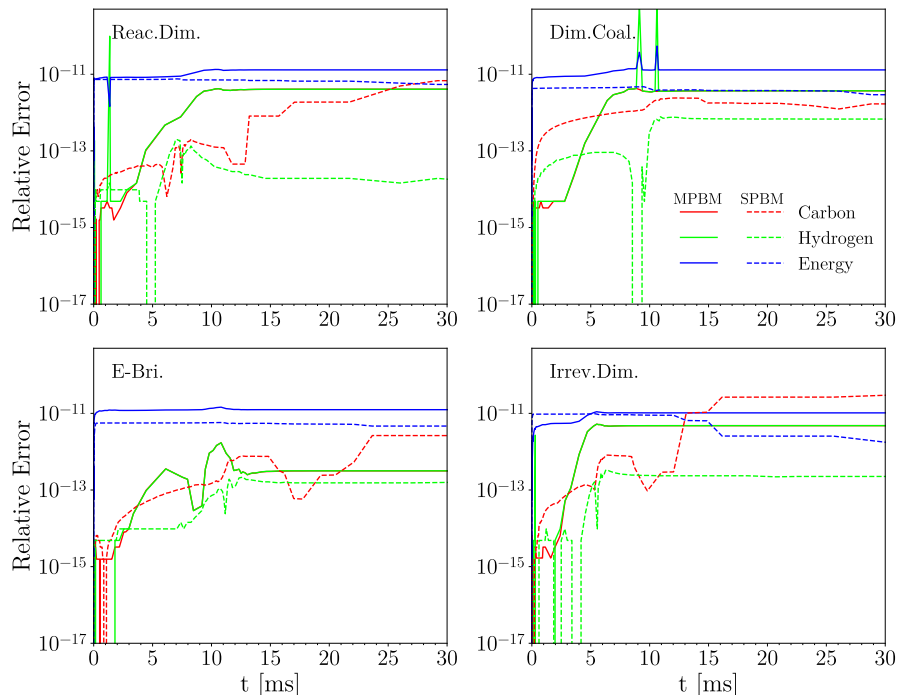


Figure 3.5: The relative error of total carbon (red line) and hydrogen (green line) mass, and total internal energy residual of gas and soot (blue line) plotted against residence time during pyrolysis of 30% CH_4 - N_2 at 2455 K and 3.47 atm in the constant volume reactor simulated using reactive dimerization, dimer coalescence, e-bridge formation and irreversible dimerization along with MPBM (solid line) and SPBM (dashed line)

3.1.4 Plug Flow Reactor

Methane pyrolysis in an adiabatic flow reactor is used to check elemental carbon and hydrogen, and energy balance in the PFR model. The inlet flow enters the reactor at the the composition of 30% CH_4 diluted in N_2 , and $T=2100$ K and $P=1$ atm. Figure 3.6 shows the residual of total elemental carbon and hydrogen, and energy up to 40 cm of the reactor length using all PAH growth and particle dynamics model. The fluctuations in residuals start at the beginning of the reactor by pyrolysis of CH_4 leading to the formation of intermediate species such and C_2H_2 and PAHs. This initiates soot inception of surface growth affecting the gas chemistry and energy that ends near $x=10$ cm, and then the coagulation of particles is dominant with no affect on mass and energy of particles.

3.2 Burner-stabilized Premixed Flames

3.3 Shock-tubes

In this section, we focus on simulation of soot formation in shock-tubes using the constant volume reactor of omnisoot, and compare species mole fraction and soot yield and morphology (if available) with benchmark measurements. Figure 3.7 (left pane) illustrates the schematics of a shock-tube

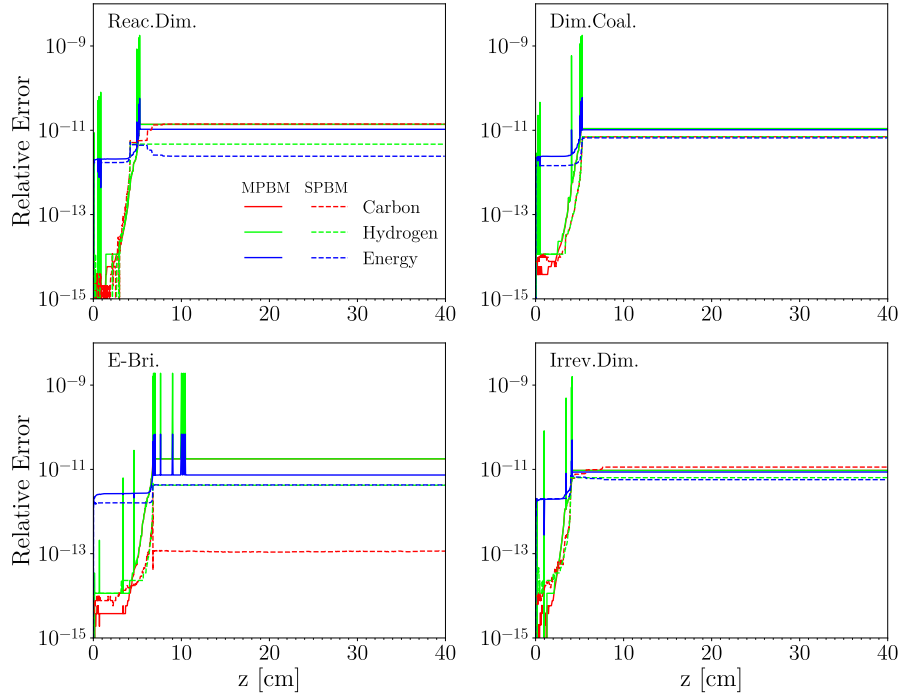


Figure 3.6: The relative error of total carbon (red line) and hydrogen (green line) mass, and total internal energy residual of gas and soot (blue line) plotted against reactor length (cm) in the adiabatic flow reactor during pyrolysis of 30% $\text{CH}_4\text{-N}_2$ at 2100 K and 1 atm simulated using reactive dimerization, dimer coalescence, e-bridge formation and irreversible dimerization along with MPBM (solid line) and SPBM (dashed line)

along with the idealized wave diagram. Shock-tubes are typically designed as a several meter long cylindrical tube separated by thin diaphragm into a smaller driver section filled a high pressure inert gas, and a longer driven section with diluted reactants. When the diaphragm is ruptured, the first shock wave propagates through the reactant mixture. The front shock compresses the reactants adiabatically raising the temperature and pressure throughout the shock-tube from T_1 , P_1 to T_2 , P_2 . The passage of the reflected shock from the end wall heats up the reactants for the second time reaching T_5 , P_5 . Figure 3.7 (right pane) shows the first and second jump in pressure due to the front and reflected shocks, respectively, and the variation in soot volume fraction during the pyrolysis of 0.03% benzene in Ar. The reflected shock creates a nearly still mixture with a constant temperature and pressure (as shown in left pane of Figure 3.7) which provides an ideal condition for kinetic studies and rate constant investigations [80]. Therefore, the use of a shock tube provides a unique opportunity for investigating the kinetics of soot formation from fuels and at various temperatures, pressures and concentrations.

However, the processes investigated in shock tubes are limited to short residence times usually 1-3 ms, so they can only be used to study early stages of soot formation such as inception and surface growth, and not for processes occurring at longer residence times such as coagulation and carbonization. Note that the residence time is calculated after the passage of reflected shock. There is a delay in the increase of volume fraction known as induction time, τ_{ind} . There has been a lot of research in the literature focused on induction time (similarly on ignition delay time) in shock tubes [103], but it is not the focus of this work. Instead, here we mainly investigate the species concentrations and soot characteristics during the pyrolysis of hydrocarbons, especially methane, at atmospheric and higher pressure which can be used for the design and optimization of carbon black in plasma reactors [104].

First, the pyrolysis of 5% and 10% CH_4 diluted with Ar is investigated for the post-shock temperature range of 1800-3000 K and the pressure range of 4.7-7.1 bar. We assume the pressure linearly increase by temperature across the simulation cases. The obtained soot yields by were compared with the soot yield measured by Agafonov et al. [105] using a dual-beam absorption-emission technique. Agafonov et al. [105] reported $\text{yield} \times E(m)$ at $\lambda = 632$ nm, and yield data was retrieved using $E(m) = 0.37$ suggested therein.

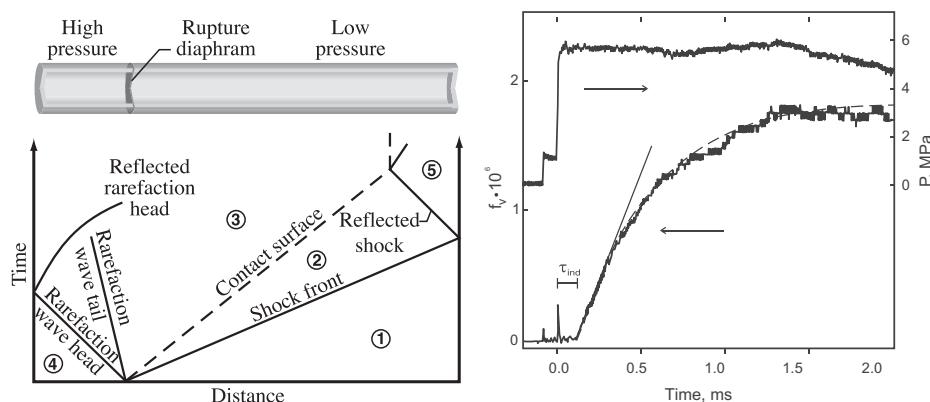


Figure 3.7: The schematics of a shock-tube and the idealized shockwave diagram(left pane reprinted from Kee et al. [80]) and the variation of soot volume fraction measured by the extinction record at 633 nm and the pressure profile behind the reflected shock wave in a mixture 0.03% benzene in Ar at $T = 1890$ K(right pane reprinted from Karasevich et al. [106])

Figure 3.8 depicts soot yield (SY) at $t = 1.5$ ms for 5% and 10% CH_4 over the temperature range of 1800-3000 K using MPBM and SPBM and different inception model and Caltech [107] mechanism. Note that, the simulations were also performed using ABF [45] and KAUST [108] mechanisms, and the results were included in Appendix****. The soot yield predictions exhibit a close agreement with measurements [105] considering the uncertainties in residence time from experiments. The model also successfully captures the bell-shape dependence of soot yield on temperature that has

been observed in a variety of hydrocarbons in shock tube [109, 110]. The particle dynamics model has minimal effect on the predicted soot yield. In the vicinity of peak soot yield, SPBM results in slightly lower yield than MPBM, but they are indistinguishable in the rest of the temperature range.

In %5 CH_4 , the SY peak temperature obtained from the model is slightly shifted towards higher temperatures ($2300 \text{ K} < T_{\text{peak}} < 2400 \text{ K}$) compared to the measurements $T_{\text{peak}} = 2200 \text{ K}$. There are noticeable differences in the behavior of PAH growth model depending on the shock-tube initial temperature. When $T < 2100 \text{ K}$, Reactive Dimerization and EBridge Formation have the highest and lowest soot yield, respectively with Dimer Coalescence predicting soot yields that always falls between Reactive and Irreversible Dimerization. However, The soot yield of EBridge Formation rapidly rises with temperature and exceeds that of Reactive Dimerization and stays higher for the rest of temperature range.

The SY noticeably increases for higher initial CH_4 mole fraction of %10 because more PAH and C_2H_2 are formed leading to stronger carbon conversion rate to soot via inception and surface growth. The peak SY obtained from the model occurs in a higher temperature range 2600-2700 K compared to %5 CH_4 . Soot yield trends can be better understood by examining carbon mass fraction of species directly contributing to soot mass. Figure 3.9 depicts the bell-shape distribution of the carbon mass fraction of soot precursors (A2, A2R5, A3, and A4) over the studied temperature range. In low ($T = 1800 \text{ K}$) and high ($T = 2300 \text{ K}$) end of distribution, a low amount of precursors are formed resulting in low inception rates, particle number concentration and surface growth sites that reduces the soot yield. Additionally, %10 CH_4 has a wider spread with peaks at higher temperature compared to %5 CH_4 which explains the shift in peak yield temperature in Figure 3.8. The effect of particle dynamics model is only noticeable in Reactive Dimerization where SPBM results in higher precursor CMF (lower consumption) due to its lower PAH adsorption rates.

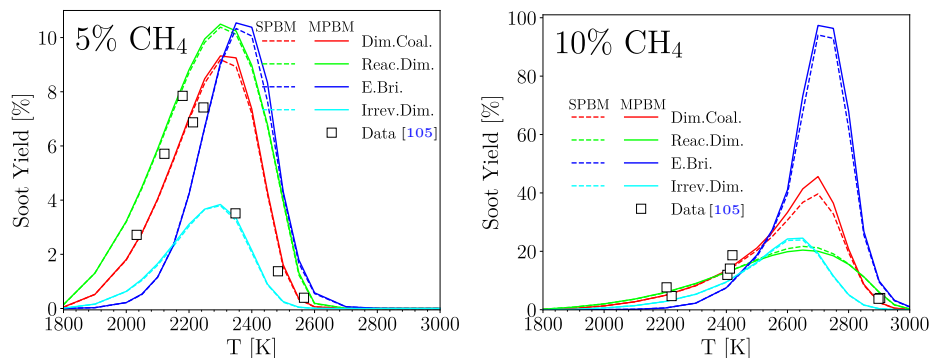


Figure 3.8: The temperature dependence of soot yield during pyrolysis of 5% CH_4 -Ar (left pane) and 10% CH_4 -Ar (right pane) at $P = 4.5\text{--}6.7 \text{ bar}$ obtained using Caltech mechanism and different inception models compared with measurements at 1.5ms [105] where the absorption function of $E(m)=0.37$ is used to estimate soot yield.

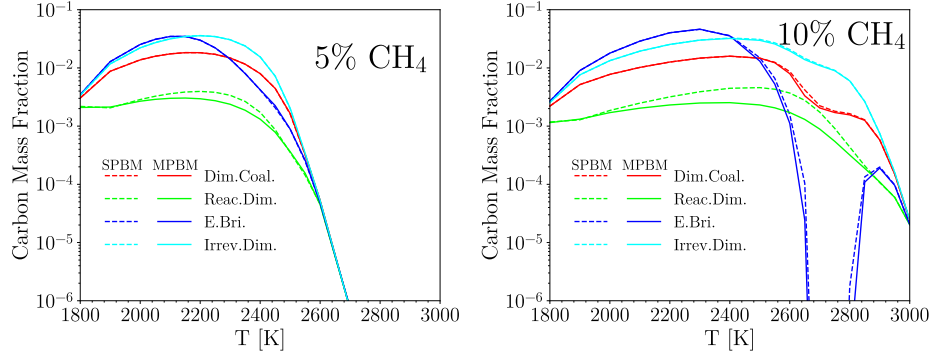


Figure 3.9: The temperature dependence of carbon mass fraction of soot precursors (A2, A2R5, A3, and A4) combined during pyrolysis of 5% CH₄-Ar (left pane) and 10% CH₄-Ar (right pane) at P = 4.5–6.7 bar obtained using Caltech mechanism and different inception models at t=1.5 ms

EBridge Formation exhibits a similar behavior in %10 CH₄ simulations where it starts with the lowest SY at T<2500 K and then quickly increases reaching its peak at 100% which is significantly larger than other PAH growth models. The remarkable drop in carbon mass fraction of precursors with EBridge Formation corresponds to %100 yield meaning that all gaseous carbon including the precursors are directed towards soot particles. The higher precursor CMF with Irreversible Dimerization near the peak yield temperature region (2200–2400 K for %5 CH₄ and 2600–2800 K for %10 CH₄) indicates less consumption of precursors via inception and PAH adsorption.

Figure 3.10 shows the CMF of C₂H₂ that has an overall increasing trend in the temperature range, but it reaches a plateau for %5 CH₄. There is also a remarkable drop in C₂H₂ CMF in 2600–2800 K due to strong mass growth rate of soot particles that drains C₂H₂ from the gas mixture leading to high soot yield $\approx 100\%$.

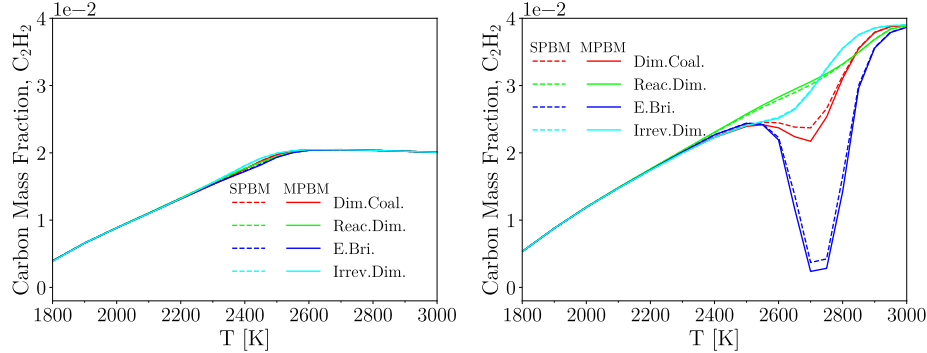


Figure 3.10: The temperature dependence of carbon mass fraction of C₂H₂ during pyrolysis of 5% CH₄-Ar (left pane) and 10% CH₄-Ar (right pane) at P = 4.5–6.7 bar obtained using Caltech mechanism and different inception models at t=1.5 ms

Although soot yield, and precursor and acetylene CMF are not sensitive to particle dynamics model, there is a significant difference in agglomerate morphology between SPBM and MPBM predictions. Fig. 3.11 shows the average number of primary particles per agglomerate, which is larger for SPBM by the maximum factor of 5 for EBridge Formation and Dimer Coalescence in 10% CH₄. SPBM predicts larger agglomerates due to accounting for polydispersity of particles that results in higher overall collision rate and faster growth by coagulation. n_p follows a bell-shape trend similar to soot yield (Fig. 3.8). The n_p values and the difference between the particle dynamics models reaches their maximum in 2200–2400 K for %5 CH₄ and 2600–2800 K for %10 CH₄ because of a stronger inception flux leading to larger number concentration of particles and higher coagulation rate. n_p is larger for Dimer Coalescence and EBridge Formation reaching the maximum of nearly

100 and 1000 in %5 and %10 CH_4 , respectively using SPBM. The effect of particle dynamics is minimum for Reactive and Irreversible Dimerization at 5% CH_4 over the whole temperature range.

Fig.3.12 shows the standard geometric deviation of mobility diameter, σ_g obtained by SPBM that reaches the maximum of 5 and 10 for %5 and %10 CH_4 , respectively indicating a significant degree of polydispersity in the generated particles at $t=1.5\text{ms}$.

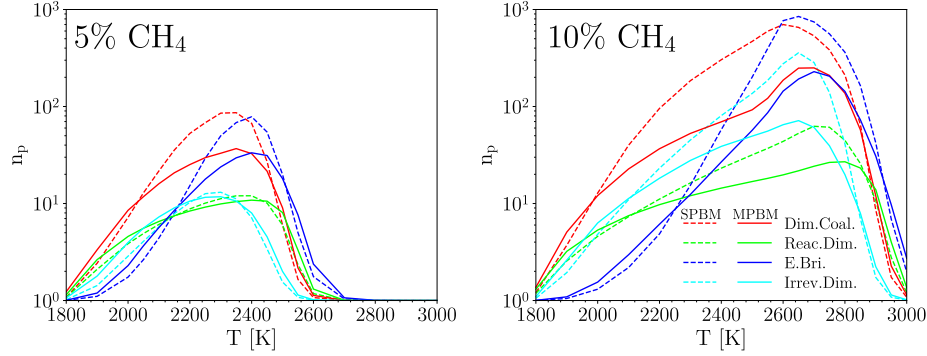


Figure 3.11: The temperature dependence of average number of primary particle per agglomerate, n_p during pyrolysis of 5% CH_4 -Ar (left pane) and 10% CH_4 -Ar (right pane) at $P = 4.5\text{--}6.7$ bar obtained using Caltech mechanism and different inception models at $t=1.5$ ms

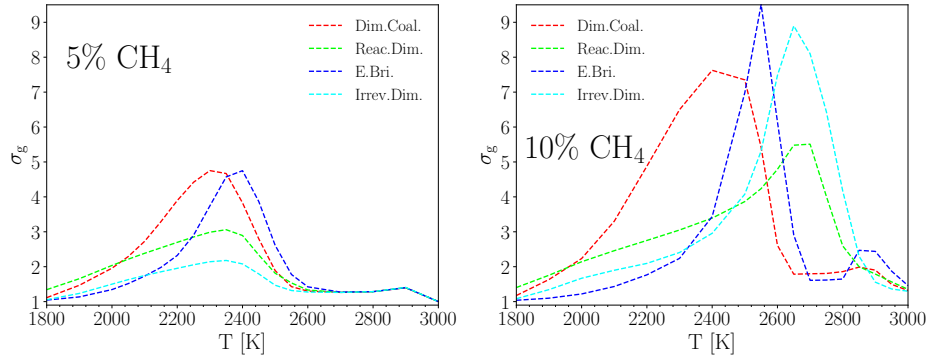


Figure 3.12: The time variation of standard geometric deviation of mobility diameter, σ_g during pyrolysis of 5% CH_4 -Ar (left pane) and 10% CH_4 -Ar (right pane) at $P = 4.5\text{--}6.7$ bar obtained using Caltech mechanism and different inception models at $t=1.5$ ms

The σ_g values from the SMPS measurements of soot particles at $t \approx 45\text{ms}$ in a benchmark burner-stabilized premixed are close to 1.1, which is significantly lower than values observed here. So, the evolution of σ_g in the studied shock tube is examined in an extended time frame up to 4 msf for 10% CH_4 at $T=2500$ and 2700 K. As shown in Fig.3.13, for all PAH growth models σ_g rises in the beginning due to simultaneous inception and coagulation that increases polydispersity and rapidly drops and approaches 1.5 before $t=3\text{ms}$ when coagulation becomes dominant and inception weakens due to consumption of precursors by PAH adsorption and HACA.

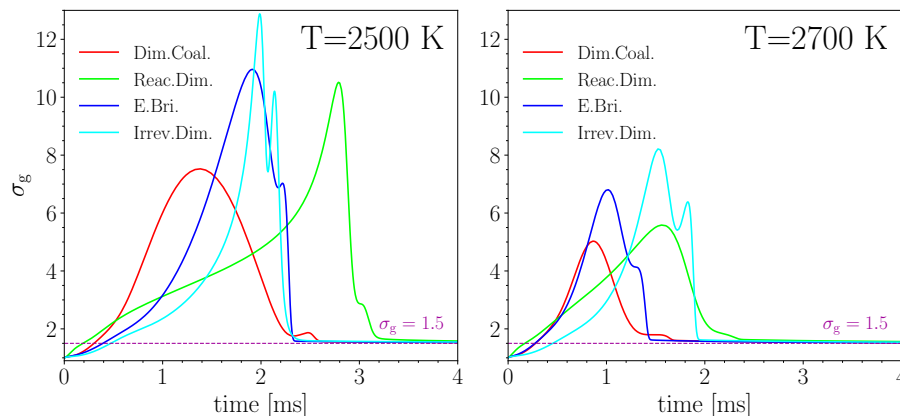


Figure 3.13: The temperature dependence of standard geometric deviation of mobility diameter, σ_g during pyrolysis of 10% CH_4 -Ar at $T=2500$ K (left pane) and $T=2700$ K (right pane)

The next set of shock tube data comes from experiments on CH_4 pyrolysis conducted by Ronald Hanson Group at Stanford University. The data has not been published yet (at the time of writing the document) and were provided through the collaboration with Monolith Materials and Stanford University.

The first data set includes eight measurements with the fuel loading of 30% CH_4 -Ar at $P=4\pm0.5$ atm in the temperature range of 1800-2500 K. The time history of CH_4 , C_2H_4 and C_2H_2 mole fraction as well as soot yield and volume fraction were reported up to 0.5 ms. Soot volume fraction was measured using light extinction at $\lambda=632$ nm with $E(m)=0.37$ [111]. The constant volume reactor was used with all PAH growth and particle dynamics models. First, the effect of gas chemistry on species and soot predictions will be examined by comparing the temperature, mole fraction of CH_4 , C_2H_2 and soot volume fraction obtained using Caltech [107], KAUST [108] and ABF [45] reaction mechanisms. Here, the comparison is done for one data point, $T=2184$ K and $P=3.62$ atm, but the extensive investigations in Appendix**** shows that the conclusions about the mechanisms are valid for the entire data set. Fig.3.14 temperature time history predicted by different PAH growth and particle dynamics models and mechanisms. All mechanisms underpredict the temperature and the discrepancy between numerical results and measurements increases with time. While the error of ABF predictions reaches a maximum of 33 K at $t=0.5$ ms, which is with acceptable range considering the experimental uncertainties, KAUST and Caltech yield the maximum error of 60 K and 102 K at the same time, respectively. As shown in Fig.3.15 and 3.15, ABF mechanism has a more accurate prediction of mole fraction of CH_4 and C_2H_2 , but Caltech and KAUST underpredict both quantities indicating that these mechanisms predict a stronger decomposition rate of CH_4 and a higher conversion of C_2H_2 to larger hydrocarbons, especially PAHs.

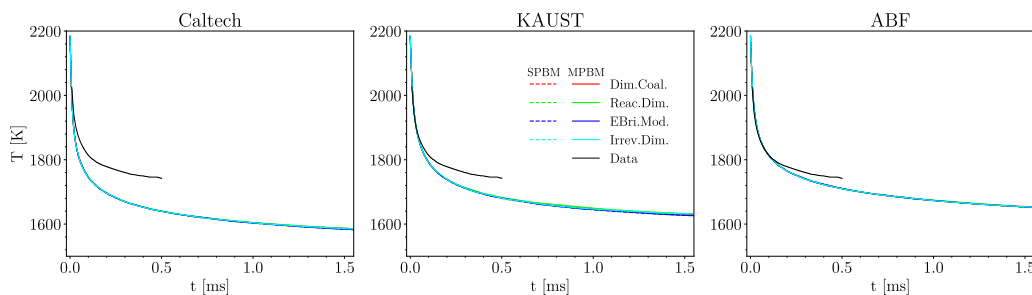


Figure 3.14: The time history of temperature of 30% CH_4 pyrolysis at $T=2184$ K and $P=3.62$ atm using Caltech, KAUST, and ABF mechanism and different PAH growth and particle dynamics models

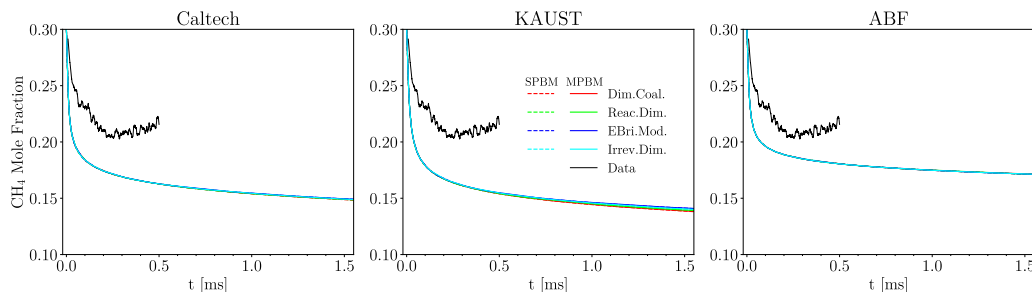


Figure 3.15: The time history of CH_4 mole fraction of 30% CH_4 pyrolysis at $T=2184$ K and $P=3.62$ atm using Caltech, KAUST, and ABF mechanism and different PAH growth and particle dynamics models

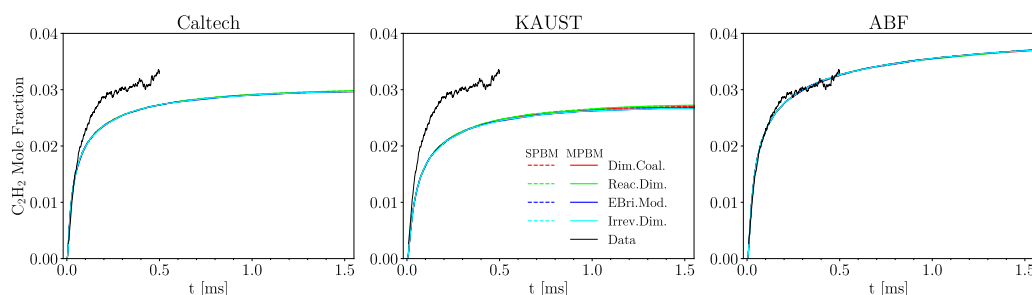


Figure 3.16: The time history of C_2H_2 mole fraction of 30% CH_4 pyrolysis at $T=2184$ K and $P=3.62$ atm using Caltech, KAUST, and ABF mechanism and different PAH growth and particle dynamics models

This is better evident in Fig. 3.15 showing CMF of CH_4 , C_2H_4 , and C_2H_2 combined. The results obtained using ABF increases after the initial decrease varying in the range of 1-0.95 indicating that most of carbon mass (>95%) remains in these three species in the studied time frame. However, CMF of the species continuously decreases with KAUST and Caltech confirming the lack/weakness of pathways driving the transfer of carbon from small to large hydrocarbon in ABF mechanism that significantly reduces the soot inception rates. Fig. 3.18 shows the soot volume fraction predicted using different models and mechanisms. ABF underpredicts f_v by more than three orders of magnitude, but KAUST and Caltech predictions are close, for some PAH growth models, exceeds the measurements. Interestingly, the combination of KAUST and Ebridge Formation perfectly matches the value and trend of experimental f_v . The mechanism comparison can be summarized as following: ABF mechanism predict more accurate temperature and the mole fraction of CH_4 and C_2H_2 , but remarkably underestimates soot volume fraction due to a low production rate of PAHs from C_2H_2 . Caltech and KAUST overestimate the endothermic decomposition of CH_4 leading to lower temperature prediction, and directs more carbon to PAHs resulting in comparable soot mass. The temperature and species mole fractions is not sensitive to PAH growth and particle dynamics models. f_v significantly changes with PAH growth model, but MPBM and SPBM predictions overlap within 1.5 ms of the simulation. As a results, only simulations by KAUST are used to examine soot morphology and composition and the effect of PAH growth models in the temperature range.

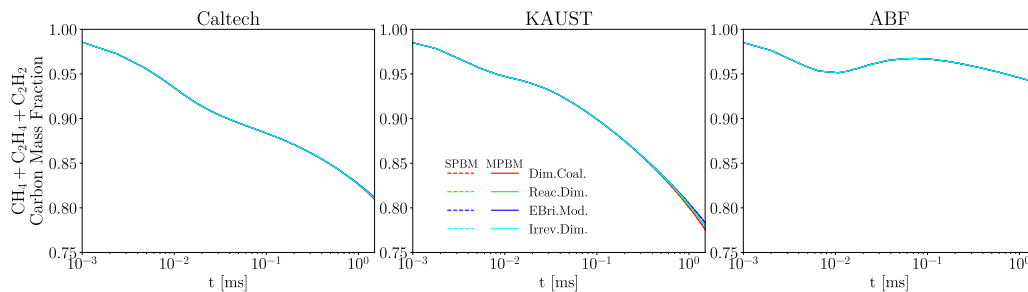


Figure 3.17: The time history of carbon mass fraction of CH_4 , C_2H_4 , and C_2H_2 of 30% CH_4 pyrolysis at $T=2184$ K and $P=3.62$ atm using Caltech, KAUST, and ABF mechanism and different PAH growth and particle dynamics models

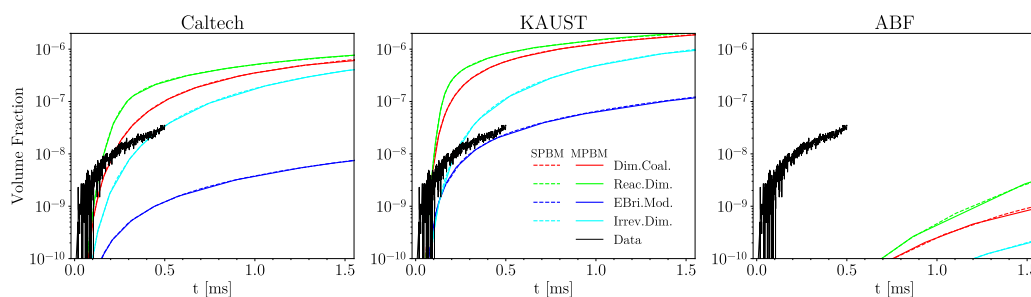


Figure 3.18: The time history of soot volume fraction of 30% CH_4 pyrolysis at $T=2184$ K and $P=3.62$ atm using Caltech, KAUST, and ABF mechanism and different PAH growth and particle dynamics models

Fig. 3.19 shows that the time variation of soot volume fraction in the temperature range of 1800–2500 K. The measurement data was not available (or too noisy) below $T=2155$ K due to lack of enough soot particle leading to weak extinction signal. In all cases with higher temperatures, EBridge Formation predicts the lowest volume fraction that interestingly are in close agreement with the data. Reactive Dimerization and Dimer Coalescence yields the largest f_v nearly two orders of magnitude higher than the measurements that start with a rapid increase indicating a stronger inception rate leading to larger number concentration of particles that provide more surface area for surface growth via HACA. Shock tube temperature increases f_v with all PAH growth models over the 1.5 ms. Moreover, high temperature accelerates soot formation, which can be examined by comparing f_v at early stages of simulation. For example, no soot appears before $t=0.25$ ms i.e. $f_v < 10^{-10}$ at $T=1861$ K, but f_v approaches 10^{-6} at $T=2455$.

Fig. 3.20 shows the time history of primary particle diameter, d_p at different temperatures. As expected, EBridge Formation and Irreversible Dimerization has the lowest d_p due to low soot mass growth rate leading to small f_v values. Although Dimer Coalescence and Reactive Dimerization generate close volume fraction values corresponding to similar soot mass, the latter predicts larger d_p indicating a lower number of N_{pri} . In other words, RD has lower inception rates and a stronger PAH adsorption rate compared to DC. The d_p by RD exhibits a noticeable sensitivity to particle dynamics model that grows with temperature. Both model predict the initial rapid rise in d_p . While MPBM predicts a gradual increase to final value, d_p by SPBM decreases for $T > 2000$ K due to stronger inception rate by SPBM that generates particle with $d_p=2$ nm bringing down the average d_p .

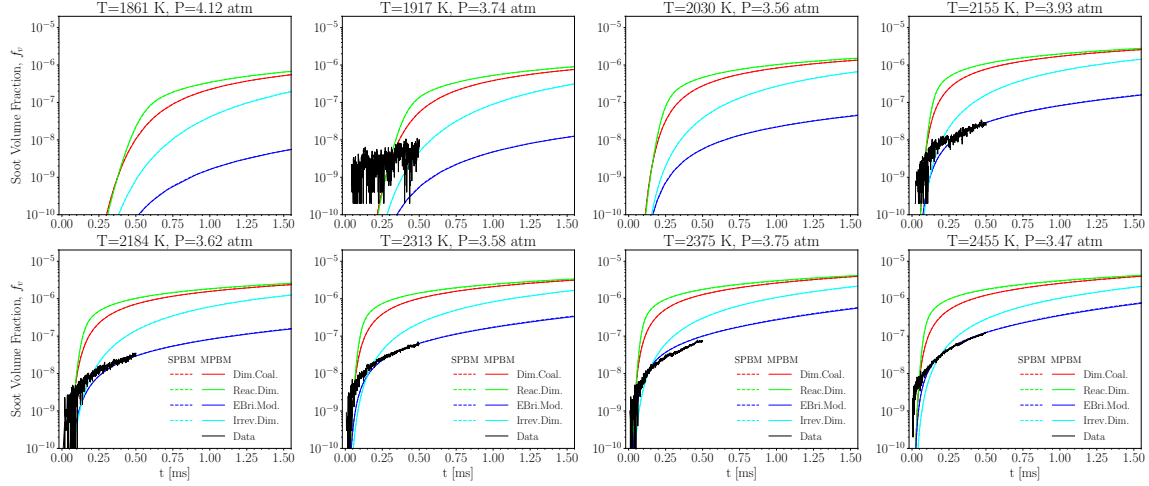


Figure 3.19: The time history of soot volume fraction of 30% CH_4 pyrolysis in the temperature range of 1800-2500 K and $P=4\pm 0.5$ atm using KAUST mechanism and different PAH growth and particle dynamics models

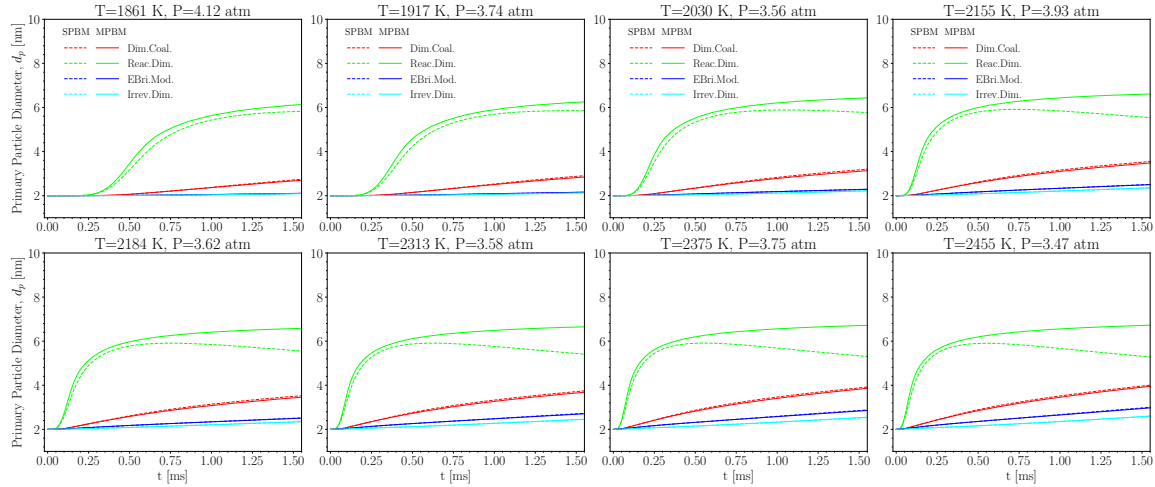


Figure 3.20: The time history of primary particle diameter, d_p of 30% CH_4 pyrolysis in the temperature range of 1800-2500 K and $P=4\pm 0.5$ atm using KAUST mechanism and different PAH growth and particle dynamics models

Fig.3.21 shows time histories d_m at different shock tube temperature. Similar to d_p , d_m increases over time and with shock tube temperature. The rise in d_m occurs faster. Initially, the generated agglomerates are small ($n_p \approx 1$), and d_m is close to d_p , so RD yield the highest d_m , but DC takes over and exceeds RD. Additionally, d_m predicted by MPBM is larger in the beginning of the simulation, but d_m predicted by SPBM rises faster at longer residence times. Fig. 3.22 shows the carbon mass growth rate by inception, HACA and PAH adsorption at $T=2455$ K and $P=3.47$ atm that explains the difference in the behavior of PAH growth and particle dynamics model in prediction of soot mass and morphology. The inception rate of RD (Fig. 3.22-a) rapidly rises reaching its peak values and quickly drops until $t=0.25$ ms when a bifurcation occurs. While the inception rate by MPBM gradually decreases, SPBM predicts an increasing rate of production of new particles leading to a smaller d_p . DC reaches the inception peak higher than other PAH growth models before $t=0.25$ ms creating more particles that causes larger d_m after coagulation becomes dominant.

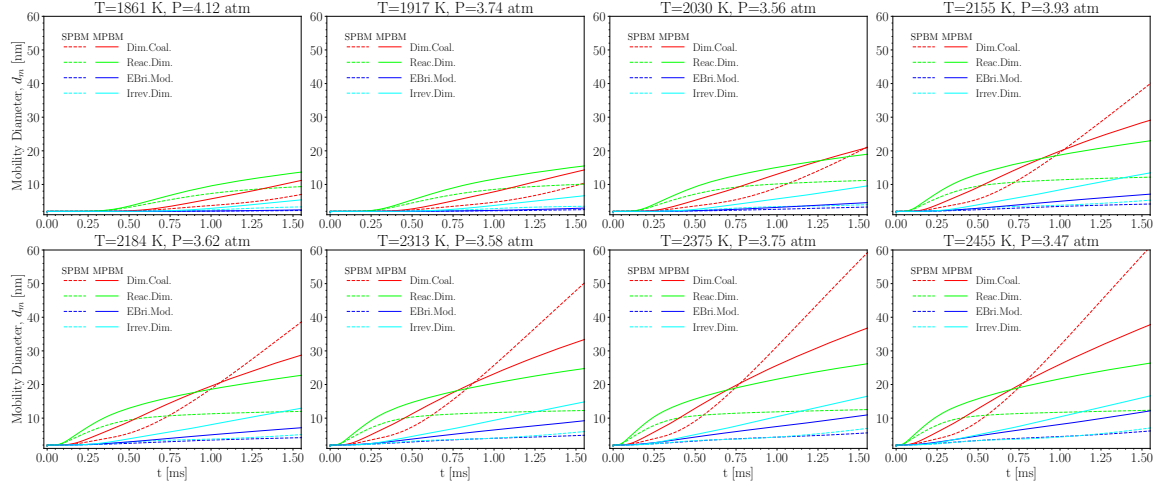


Figure 3.21: The time history of mobility diameter, d_m of 30% CH_4 pyrolysis in the temperature range of 1800-2500 K and $P=4\pm 0.5$ atm using KAUST mechanism and different PAH growth and particle dynamics models

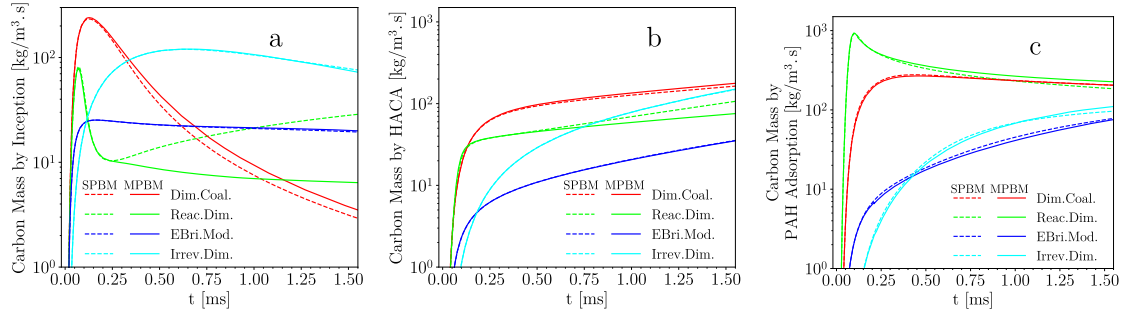


Figure 3.22: The time history of carbon mass gained by inception(a), HACA (b), and PAH adsorption (c) of pyrolysis of 30% CH_4 at $T=2455$ K and $P=3.47$ atm using KAUST mechanism and different PAH growth and particle dynamics models

Bibliography

- [1] Gunnar Myhre, Drew Shindell, and Julia Pongratz. Anthropogenic and natural radiative forcing. 2014.
- [2] World Health Organization et al. Health effects of particulate matter: Policy implications for countries in eastern europe, caucasus and central asia. 2013.
- [3] U.S. EPA. Integrated science assessment (isa) for particulate matter (final report, dec 2019). 2019.
- [4] Ann Y Watson and Peter A Valberg. Carbon black and soot: two different substances. *AIHA-J-American Industrial Hygiene Association*, 62(2):218–228, 2001.
- [5] International Carbon Black Association et al. Carbon black user’s guide. *available at www.carbon-black.org*, 2016.
- [6] Verónica Palomares, Aintzane Goñi, Izaskun Gil De Muro, Iratxe De Meatza, Miguel Bengoechea, Igor Cantero, and Teófilo Rojo. Conductive additive content balance in li-ion battery cathodes: Commercial carbon blacks vs. in situ carbon from lifepo4/c composites. *J. Power Sources*, 195:7661–7668, 2010. ISSN 0378-7753.
- [7] Sotiris E Pratsinis. History of manufacture of fine particles in high-temperature aerosol reactors. *Aerosol science and technology: History and reviews*, pages 475–507, 2011.
- [8] Roop Chand Bansal, Meng-Jiao Wang, and JB Donnet. Carbon black. *Science and Technology*, 133, 1993.
- [9] Wonihl Cho, Seung-Ho Lee, Woo-Sung Ju, Youngsoon Baek, and Joong Kee Lee. Conversion of natural gas to hydrogen and carbon black by plasma and application of plasma carbon black. *Catalysis Today*, 98(4):633–638, 2004.
- [10] Soo-Jin Park, Min-Kang Seo, and Changwoon Nah. Influence of surface characteristics of carbon blacks on cure and mechanical behaviors of rubber matrix compoundings. *Journal of colloid and interface science*, 291(1):229–235, 2005.
- [11] C Russo, A Tregrossi, and A Ciajolo. Dehydrogenation and growth of soot in premixed flames. *Proceedings of the Combustion Institute*, 35(2):1803–1809, 2015.
- [12] Madhu Singh and Randy L Vander Wal. Nanostructure quantification of carbon blacks. *C*, 5(1):2, 2018.
- [13] Randy L Vander Wal, Aleksey Yezerets, Neal W Currier, Do Heui Kim, and Chong Min Wang. Hrtem study of diesel soot collected from diesel particulate filters. *Carbon*, 45(1):70–77, 2007.
- [14] Magín Lapuerta, Javier Barba, Anton D Sediako, Mohammad Reza Kholghy, and Murray J Thomson. Morphological analysis of soot agglomerates from biodiesel surrogates in a coflow burner. *Journal of Aerosol Science*, 111:65–74, 2017.

- [15] Andrea D’Anna. Combustion-formed nanoparticles. *Proceedings of the Combustion Institute*, 32(1):593–613, 2009.
- [16] Hai Wang. Formation of nascent soot and other condensed-phase materials in flames. *Proc Combust Inst.*, 33:41–67, 2011. ISSN 15407489.
- [17] Kevin Gleason, Francesco Carbone, and Alessandro Gomez. Effect of temperature on soot inception in highly controlled counterflow ethylene diffusion flames. *Combustion and Flame*, 192:283–294, 2018.
- [18] Kevin Gleason, Francesco Carbone, and Alessandro Gomez. Paks controlling soot nucleation in 0.101–0.811 mpa ethylene counterflow diffusion flames. *Combustion and Flame*, 227:384–395, 2021.
- [19] Beat Buesser and Sotiris E Pratsinis. Design of nanomaterial synthesis by aerosol processes. *Annual review of chemical and biomolecular engineering*, 3:103–127, 2012.
- [20] Jacob W Martin, Maurin Salamanca, and Markus Kraft. Soot inception: Carbonaceous nanoparticle formation in flames. *Progress in Energy and Combustion Science*, 88:100956, 2022.
- [21] Stephen E Stein and A Fahr. High-temperature stabilities of hydrocarbons. *The Journal of Physical Chemistry*, 89(17):3714–3725, 1985.
- [22] A Oberlin. Carbonization and graphitization. *Carbon*, 22:521–541, 1984. ISSN 0008-6223.
- [23] Joaquin Camacho, Changran Liu, Chen Gu, He Lin, Zhen Huang, Quanxi Tang, Xiaoqing You, Chiara Saggese, Yang Li, Heejung Jung, et al. Mobility size and mass of nascent soot particles in a benchmark premixed ethylene flame. *Combustion and Flame*, 162(10):3810–3822, 2015.
- [24] Steffen Salenbauch, Alberto Cuoci, Alessio Frassoldati, Chiara Saggese, Tiziano Faravelli, and Christian Hasse. Modeling soot formation in premixed flames using an extended conditional quadrature method of moments. *Combustion and Flame*, 162(6):2529–2543, 2015.
- [25] Pascale Desgroux, Alessandro Faccineto, Xavier Mercier, Thomas Mouton, Damien Aubagnac Karkar, and Abderrahman El Bakali. Comparative study of the soot formation process in a “nucleation” and a “sooting” low pressure premixed methane flame. *Combustion and Flame*, 184:153–166, 2017.
- [26] Yu Wang, Abhijeet Raj, and Suk Ho Chung. Soot modeling of counterflow diffusion flames of ethylene-based binary mixture fuels. *Combustion and Flame*, 162(3):586–596, 2015.
- [27] Lei Xu, Fuwu Yan, Mengxiang Zhou, and Yu Wang. An experimental and modeling study on sooting characteristics of laminar counterflow diffusion flames with partial premixing. *Energy*, 218:119479, 2021.
- [28] Mohammad Reza Kholghy, Armin Veshkini, and Murray John Thomson. The core-shell internal nanostructure of soot—a criterion to model soot maturity. *Carbon*, 100:508–536, 2016.
- [29] Armin Veshkini, Seth B Dworkin, and Murray J Thomson. Understanding soot particle size evolution in laminar ethylene/air diffusion flames using novel soot coalescence models. *Combustion Theory and Modelling*, 20(4):707–734, 2016.
- [30] Michael Frenklach and Hai Wang. Detailed modeling of soot particle nucleation and growth. In *Symposium (International) on Combustion*, volume 23, pages 1559–1566. Elsevier, 1991.
- [31] G Blanquart and H Pitsch. Analyzing the effects of temperature on soot formation with a joint volume-surface-hydrogen model. *Combustion and Flame*, 156(8):1614–1626, 2009.

- [32] J Houston Miller, Kermit C Smyth, and W Gary Mallard. Calculations of the dimerization of aromatic hydrocarbons: Implications for soot formation. In *Symposium (International) on Combustion*, volume 20, pages 1139–1147. Elsevier, 1985.
- [33] Hassan Sabbah, Ludovic Biennier, Stephen J Klippenstein, Ian R Sims, and Bertrand R Rowe. Exploring the role of pahs in the formation of soot: Pyrene dimerization. *The Journal of Physical Chemistry Letters*, 1(19):2962–2967, 2010.
- [34] Ali Naseri, M Reza Kholghy, Neil A Juan, and Murray J Thomson. Simulating yield and morphology of carbonaceous nanoparticles during fuel pyrolysis in laminar flow reactors enabled by reactive inception and aromatic adsorption. *Combustion and Flame*, 237:111721, 2022.
- [35] Nazly E Sanchez, Alicia Callejas, Angela Millera, Rafael Bilbao, and Maria U Alzueta. Polycyclic aromatic hydrocarbon (pah) and soot formation in the pyrolysis of acetylene and ethylene: effect of the reaction temperature. *Energy & fuels*, 26(8):4823–4829, 2012.
- [36] Sanghwan Cho, Seunghoon Lee, Wonnam Lee, and Sunho Park. Synthesis of primary-particle-size-tuned soot particles by controlled pyrolysis of hydrocarbon fuels. *Energy & Fuels*, 30(8):6614–6619, 2016.
- [37] Meghdad Saffaripour, Armin Veshkini, Mohammadreza Kholghy, and Murray J Thomson. Experimental investigation and detailed modeling of soot aggregate formation and size distribution in laminar coflow diffusion flames of jet a-1, a synthetic kerosene, and n-decane. *Combustion and Flame*, 161(3):848–863, 2014.
- [38] J Houston Miller. The kinetics of polynuclear aromatic hydrocarbon agglomeration in flames. In *Symposium (International) on Combustion*, volume 23, pages 91–98. Elsevier, 1991.
- [39] Anna Giordana, Andrea Maranzana, and Glaucio Tonachini. Theoretical investigation of soot nanoparticle inception via polycyclic aromatic hydrocarbon coagulation (condensation): Energetic, structural, and electronic features. *The Journal of Physical Chemistry C*, 115(5):1732–1739, 2011.
- [40] NA Eaves, SB Dworkin, and MJ Thomson. The importance of reversibility in modeling soot nucleation and condensation processes. *Proceedings of the Combustion Institute*, 35(2):1787–1794, 2015.
- [41] Mohammad Reza Kholghy, Nick Anthony Eaves, Armin Veshkini, and Murray John Thomson. The role of reactive pah dimerization in reducing soot nucleation reversibility. *Proceedings of the Combustion Institute*, 37(1):1003–1011, 2019.
- [42] Mohammad R Kholghy, Georgios A Kelesidis, and Sotiris E Pratsinis. Reactive polycyclic aromatic hydrocarbon dimerization drives soot nucleation. *Physical Chemistry Chemical Physics*, 20(16):10926–10938, 2018.
- [43] Michael Frenklach and Alexander M Mebel. On the mechanism of soot nucleation. *Physical Chemistry Chemical Physics*, 22(9):5314–5331, 2020.
- [44] Aamir D Abid, Joaquin Camacho, David A Sheen, and Hai Wang. Quantitative measurement of soot particle size distribution in premixed flames—the burner-stabilized stagnation flame approach. *Combustion and Flame*, 156(10):1862–1870, 2009.
- [45] Jörg Appel, Henning Bockhorn, and Michael Frenklach. Kinetic modeling of soot formation with detailed chemistry and physics: laminar premixed flames of c2 hydrocarbons. *Combustion and flame*, 121(1-2):122–136, 2000.
- [46] IT Woods and BS Haynes. Soot surface growth at active sites. *Combustion and flame*, 85(3-4):523–525, 1991.

- [47] Cameron J Dasch. The decay of soot surface growth reactivity and its importance in total soot formation. *Combustion and flame*, 61(3):219–225, 1985.
- [48] Jasdeep Singh, Robert IA Patterson, Markus Kraft, and Hai Wang. Numerical simulation and sensitivity analysis of detailed soot particle size distribution in laminar premixed ethylene flames. *Combustion and Flame*, 145(1-2):117–127, 2006.
- [49] Hope A Michelsen, Meredith B Colket, Per-Erik Bengtsson, Andrea D’anna, Pascale Desgroux, Brian S Haynes, J Houston Miller, Graham J Nathan, Heinz Pitsch, and Hai Wang. A review of terminology used to describe soot formation and evolution under combustion and pyrolytic conditions. *ACS nano*, 14(10):12470–12490, 2020.
- [50] OI Obolensky, VV Semenikhina, AV Solov’Yov, and W Greiner. Interplay of electrostatic and van der waals forces in coronene dimer. *International Journal of Quantum Chemistry*, 107(6):1335–1343, 2007.
- [51] Eirini Goudeli, Maximilian L Eggersdorfer, and Sotiris E Pratsinis. Coagulation of agglomerates consisting of polydisperse primary particles. *Langmuir*, 32:9276–9285, 2016. ISSN 0743-7463.
- [52] FS Lai, SK Friedlander, J Pich, and GM Hidy. The self-preserving particle size distribution for brownian coagulation in the free-molecule regime. *Journal of Colloid and Interface Science*, 39(2):395–405, 1972.
- [53] Raymond D Mountain, George W Mulholland, and Howard Baum. Simulation of aerosol agglomeration in the free molecular and continuum flow regimes. *Journal of Colloid and Interface Science*, 114(1):67–81, 1986.
- [54] Georgios A. Kelesidis, Eirini Goudeli, and Sotiris E. Pratsinis. Morphology and mobility diameter of carbonaceous aerosols during agglomeration and surface growth. *Carbon*, 121:527–535, 9 2017. ISSN 00086223.
- [55] Georgios A Kelesidis and Eirini Goudeli. Self-preserving size distribution and collision frequency of flame-made nanoparticles in the transition regime. *Proceedings of the Combustion Institute*, 38(1):1233–1240, 2021.
- [56] Georgios A. Kelesidis, Eirini Goudeli, and Sotiris E. Pratsinis. Flame synthesis of functional nanostructured materials and devices: Surface growth and aggregation. *Proc Combust Inst* ., 36:29–50, 2017. ISSN 15407489.
- [57] Georgios A Kelesidis and Sotiris E Pratsinis. A perspective on gas-phase synthesis of nano-materials: Process design, impact and outlook. *Chemical Engineering Journal*, 421:129884, 2021.
- [58] Yun Xiong and Sotiris E Pratsinis. Formation of agglomerate particles by coagulation and sintering—part i. a two-dimensional solution of the population balance equation. *J. Aerosol Sci.*, 24:283–300, 1993. ISSN 0021-8502.
- [59] SH Park, SN Rogak, WK Bushe, JZ Wen, and MJ Thomson. An aerosol model to predict size and structure of soot particles. *Combustion Theory and Modelling*, 9(3):499–513, 2005.
- [60] MA Schiener and RP Lindstedt. Transported probability density function based modelling of soot particle size distributions in non-premixed turbulent jet flames. *Proceedings of the Combustion Institute*, 37(1):1049–1056, 2019.
- [61] Themis Matsoukas and Sheldon K Friedlander. Dynamics of aerosol agglomerate formation. *Journal of Colloid and Interface Science*, 146(2):495–506, 1991.
- [62] MD Smooke, MB Long, BC Connelly, MB Colket, and RJ Hall. Soot formation in laminar diffusion flames. *Combustion and Flame*, 143(4):613–628, 2005.

- [63] Damien Aubagnac-Karkar, Abderrahman El Bakali, and Pascale Desgroux. Soot particles inception and pah condensation modelling applied in a soot model utilizing a sectional method. *Combustion and Flame*, 189:190–206, 2018.
- [64] Andrei Kazakov and Michael Frenklach. Dynamic modeling of soot particle coagulation and aggregation: Implementation with the method of moments and application to high-pressure laminar premixed flames. *Combustion and flame*, 114(3-4):484–501, 1998.
- [65] F Einar Kruis, Karl A Kusters, Sotiris E Pratsinis, and Brian Scarlett. A simple model for the evolution of the characteristics of aggregate particles undergoing coagulation and sintering. *Aerosol science and technology*, 19(4):514–526, 1993.
- [66] Patrick T Spicer, Olivier Chaoul, Stavros Tsantilis, and Sotiris E Pratsinis. Titania formation by ticl₄ gas phase oxidation, surface growth and coagulation. *J. Aerosol Sci.*, 33:17–34, 2002. ISSN 0021-8502.
- [67] Georgios A Kelesidis and Sotiris E Pratsinis. Estimating the internal and surface oxidation of soot agglomerates. *Combustion and Flame*, 209:493–499, 2019.
- [68] Aamir D Abid, Nicholas Heinz, Erik D Tolmachoff, Denis J Phares, Charles S Campbell, and Hai Wang. On evolution of particle size distribution functions of incipient soot in premixed ethylene–oxygen–argon flames. *Combustion and Flame*, 154(4):775–788, 2008.
- [69] X Ma, CD Zangmeister, and MR Zachariah. Soot oxidation kinetics: a comparison study of two tandem ion-mobility methods. *The Journal of Physical Chemistry C*, 117(20):10723–10729, 2013.
- [70] Arto J Gröhn, Sotiris E Pratsinis, and Karsten Wegner. Fluid-particle dynamics during combustion spray aerosol synthesis of zro₂. *Chemical Engineering Journal*, 191:491–502, 2012.
- [71] Sotiris E Pratsinis. Simultaneous nucleation, condensation, and coagulation in aerosol reactors. *Journal of colloid and interface science*, 124(2):416–427, 1988.
- [72] Guillaume Blanquart and Heinz Pitsch. A joint volume-surface-hydrogen multi-variate model for soot formation. *Combustion generated fine carbonaceous particles*, pages 437–463, 2009.
- [73] Kyo-Seon Kim and Sotiris E Pratsinis. Manufacture of optical waveguide preforms by modified chemical vapor deposition. *AIChE journal*, 34(6):912–921, 1988.
- [74] Michael Frenklach and Stephen J Harris. Aerosol dynamics modeling using the method of moments. *Journal of colloid and interface science*, 118(1):252–261, 1987.
- [75] Stavros Tsantilis and Sotiris E Pratsinis. Soft-and hard-agglomerate aerosols made at high temperatures. *Langmuir*, 20(14):5933–5939, 2004.
- [76] Peter R Lindstedt. Simplified soot nucleation and surface growth steps for non-premixed flames. In *Soot formation in combustion: mechanisms and models*, pages 417–441. Springer, 1994.
- [77] Robert N Grass, Stavros Tsantilis, and Sotiris E Pratsinis. Design of high-temperature, gas-phase synthesis of hard or soft tio₂ agglomerates. *AIChE Journal*, 52(4):1318–1325, 2006.
- [78] Kirk A Jensen, Jill M Suo-Anttila, and Linda G Blevins. Measurement of soot morphology, chemistry, and optical properties in the visible and near-infrared spectrum in the flame zone and overfire region of large jp-8 pool fires. *Combustion science and technology*, 179(12):2453–2487, 2007.
- [79] Bonnie J McBride. *Coefficients for calculating thermodynamic and transport properties of individual species*, volume 4513. National Aeronautics and Space Administration, Office of Management . . . , 1993.

- [80] Robert J Kee, Michael E Coltrin, Peter Glarborg, and Huayang Zhu. *Chemically reacting flow: theory, modeling, and simulation*. John Wiley & Sons, 2017.
- [81] David G. Goodwin, Harry K. Moffat, Ingmar Schoegl, Raymond L. Speth, and Bryan W. Weber. Cantera: An object-oriented software toolkit for chemical kinetics, thermodynamics, and transport processes. <https://www.cantera.org>, 2022. Version 2.6.0.
- [82] George W Mulholland, RJ Samson, RD Mountain, and MH Ernst. Cluster size distribution for free molecular agglomeration. *Energy & Fuels*, 2(4):481–486, 1988.
- [83] RC Ball and R Jullien. Finite size effects in cluster-cluster aggregation. *Journal de Physique Lettres*, 45(21):1031–1035, 1984.
- [84] Jérôme Yon, A Bescond, and F-X Ouf. A simple semi-empirical model for effective density measurements of fractal aggregates. *Journal of Aerosol Science*, 87:28–37, 2015.
- [85] Jenny Rissler, Maria E Messing, Azhar I Malik, Patrik T Nilsson, Erik Z Nordin, Mats Bohgard, Mehri Sanati, and Joakim H Pagels. Effective density characterization of soot agglomerates from various sources and comparison to aggregation theory. *Aerosol Science and Technology*, 47(7):792–805, 2013.
- [86] Anna Ciajolo, Rosalba Barbella, Antonio Tregrossi, and Loretta Bonfanti. Spectroscopic and compositional signatures of pah-loaded mixtures in the soot inception region of a premixed ethylene flame. In *Symposium (International) on Combustion*, volume 27, pages 1481–1487. Elsevier, 1998.
- [87] Christopher Betrancourt, Fengshan Liu, Pascale Desgroux, Xavier Mercier, Alessandro Facinetto, Maurin Salamanca, Lena Ruwe, Katharina Kohse-Höinghaus, Daniel Emmrich, André Beyer, et al. Investigation of the size of the incandescent incipient soot particles in premixed sooting and nucleation flames of n-butane using lii, him, and 1 nm-smgs. *Aerosol Science and Technology*, 51(8):916–935, 2017.
- [88] Hope A Michelsen. Probing soot formation, chemical and physical evolution, and oxidation: A review of in situ diagnostic techniques and needs. *Proceedings of the Combustion Institute*, 36(1):717–735, 2017.
- [89] Nikolaj A Fuchs, RE Daisley, Marina Fuchs, CN Davies, and ME Straumanis. The mechanics of aerosols, 1965.
- [90] Jin Jwang Wu and Richard C Flagan. A discrete-sectional solution to the aerosol dynamic equation. *Journal of Colloid and interface Science*, 123(2):339–352, 1988.
- [91] BS Haynes and H Gg Wagner. The surface growth phenomenon in soot formation. *Zeitschrift für Physikalische Chemie*, 133(2):201–213, 1982.
- [92] Stephen J Harris and Anita M Weiner. Chemical kinetics of soot particle growth. *Annual Review of Physical Chemistry*, 36(1):31–52, 1985.
- [93] KH Homann. Formation of large molecules, particulates and ions in premixed hydrocarbon flames; progress and unresolved questions. In *Symposium (International) on Combustion*, volume 20, pages 857–870. Elsevier, 1985.
- [94] Armin Veshkini. *Understanding Soot Particle Growth Chemistry and Particle Sizing Using a Novel Soot Growth and Formation Model*. University of Toronto (Canada), 2015.
- [95] K Olof Johansson, Tyler Dillstrom, Matteo Monti, Farid El Gabaly, Matthew F Campbell, Paul E Schrader, Denisia M Popolan-Vaida, Nicole K Richards-Henderson, Kevin R Wilson, Angela Violi, et al. Formation and emission of large furans and oxygenated hydrocarbons from flames. *Proceedings of the National Academy of Sciences*, 113(30):8374–8379, 2016.

- [96] J Houston Miller, W Gary Mallard, and Kermit C Smyth. Intermolecular potential calculations for polycyclic aromatic hydrocarbons. *The Journal of Physical Chemistry*, 88(21):4963–4970, 1984.
- [97] Yoichiro Araki, Yoshiya Matsukawa, Yasuhiro Saito, Yohsuke Matsushita, Hideyuki Aoki, Koki Era, and Takayuki Aoki. Effects of carrier gas on the properties of soot produced by ethylene pyrolysis. *Fuel Processing Technology*, 213:106673, 2021.
- [98] Binxuan Sun, Stelios Rigopoulos, and Anxiong Liu. Modelling of soot coalescence and aggregation with a two-population balance equation model and a conservative finite volume method. *Combustion and Flame*, 229:111382, 2021.
- [99] A Tregrossi, A Ciajolo, and R Barbella. The combustion of benzene in rich premixed flames at atmospheric pressure. *Combustion and flame*, 117(3):553–561, 1999.
- [100] Eirini Goudeli, Maximilian L Eggersdorfer, and Sotiris E Pratsinis. Coagulation–agglomeration of fractal-like particles: Structure and self-preserving size distribution. *Langmuir*, 31(4):1320–1327, 2015.
- [101] M Reza Kholghy and Georgios A Kelesidis. Surface growth, coagulation and oxidation of soot by a monodisperse population balance model. *Combustion and Flame*, 227:456–463, 2021.
- [102] Srinivas Vemury and Sotiris E Pratsinis. Self-preserving size distributions of agglomerates. *Journal of Aerosol Science*, 26(2):175–185, 1995.
- [103] DE Fussey, AJ Gosling, and D Lampard. A shock-tube study of induction times in the formation of carbon particles by pyrolysis of the c2 hydrocarbons. *Combustion and Flame*, 32:181–192, 1978.
- [104] Laurent Fulcheri, Vandad-Julien Rohani, Elliott Wyse, Ned Hardman, and Enoch Dames. An energy-efficient plasma methane pyrolysis process for high yields of carbon black and hydrogen. *International Journal of Hydrogen Energy*, 48(8):2920–2928, 2023.
- [105] GL Agafonov, IV Bilera, PA Vlasov, IV Zhil'tsova, Yu A Kolbanovskii, VN Smirnov, and AM Tereza. Unified kinetic model of soot formation in the pyrolysis and oxidation of aliphatic and aromatic hydrocarbons in shock waves. *Kinetics and Catalysis*, 57:557–572, 2016.
- [106] Yu Karasevich, D Tanke, M Tappe, Th Thienel, H Gg Wagner, et al. Soot formation at elevated pressures and carbon concentrations in hydrocarbon pyrolysis. In *Symposium (International) on Combustion*, volume 25, pages 627–634. Elsevier, 1994.
- [107] G Blanquart, P Pepiot-Desjardins, and H Pitsch. Chemical mechanism for high temperature combustion of engine relevant fuels with emphasis on soot precursors. *Combustion and Flame*, 156(3):588–607, 2009.
- [108] Yu Wang, Abhijeet Raj, and Suk Ho Chung. A pah growth mechanism and synergistic effect on pah formation in counterflow diffusion flames. *Combustion and flame*, 160(9):1667–1676, 2013.
- [109] H Kellerer, A Müller, H-J Bauer, and S Wittig. Soot formation in a shock tube under elevated pressure conditions. *Combustion science and technology*, 113(1):67–80, 1996.
- [110] V Gg Knorre, Dietmar Tanke, Th Thienel, and H Gg Wagner. Soot formation in the pyrolysis of benzene/acetylene and acetylene/hydrogen mixtures at high carbon concentrations. In *Symposium (international) on combustion*, volume 26, pages 2303–2310. Elsevier, 1996.
- [111] GL Agafonov, IV Bilera, PA Vlasov, Yu A Kolbanovskii, VN Smirnov, and AM Tereza. Soot formation during the pyrolysis and oxidation of acetylene and ethylene in shock waves. *Kinetics and Catalysis*, 56:12–30, 2015.

Appendix A

Derivation of Transport Equations

This chapter explains the derivation of transport equations from first principles for mass, species, energy and soot variables for the reactors employed in omnisoort. The conventional reactor transport equation have been derived for a reacting gas without solid particle [80], so we provide a step by step derivation of equations that describes transport/evolution of mass, species and energy of gas as well as those of soot variables.

A.1 Constant Volume Reactor

A.1.1 Continuity

The rate change of mass of gas mixture is equal to the production rate of soot.

$$\frac{d}{dt}(m) = V(1 - \varphi) \sum_i \dot{s}_i W_i,$$

where V is the reactor volume that stays constant during the process, and gas occupies a fraction of volume reactor without soot, so $m = \rho V(1 - \varphi)$.

$$\begin{aligned} \frac{d}{dt}(\rho V(1 - \varphi)) &= V(1 - \varphi) \sum_i \dot{s}_i W_i \\ \Downarrow \\ \frac{d}{dt}(\rho(1 - \varphi)) &= (1 - \varphi) \sum_i \dot{s}_i W_i \end{aligned} \tag{A.1}$$

A.1.2 Species

The rate change of mass of each species can be described as:

$$\frac{d}{dt}(m_k) = V(1 - \varphi)(\dot{\omega}_k + \dot{s}_k)W_k$$

The mass of each species is defined as the total gas mass multiplied by the mass fraction as

$$\frac{dY_k}{dt} \rho V(1 - \varphi) + Y_k \frac{d}{dt}(\rho V(1 - \varphi)) = V(1 - \varphi)(\dot{\omega}_k + \dot{s}_k)W_k$$

where the colored term can be substituted from Equation (A.1).

$$\frac{dY_k}{dt} \rho V(1 - \varphi) + Y_k V(1 - \varphi) \sum_i \dot{s}_i W_i = V(1 - \varphi)(\dot{\omega}_k + \dot{s}_k)W_k$$

$$\Downarrow \times \frac{1}{\rho V(1-\varphi)}$$

$$\frac{dY_k}{dt} = \frac{1}{\rho} \left[(\dot{\omega}_k + \dot{s}_k) W_k - Y_k \sum_i \dot{s}_i W_i \right] \quad (\text{A.2})$$

A.1.3 Energy

In the constant volume reactor, the internal energy is favorable since the external boundaries of the control volume are not changed, and the work from soot volume is neglected, so formulating the energy balance based on the internal energy is preferred. The energy passes through the boundaries of the control volume via soot generation and external heat source.

$$\frac{dE}{dt} = -\frac{dE_{soot}}{dt} + \dot{Q}$$

$$\Downarrow E = m \sum Y_k e_k$$

$$\frac{dm}{dt} \sum_k Y_k e_k + m \sum_k \frac{dY_k}{dt} e_k + m \sum_k Y_k \frac{de_k}{dt} = -\frac{dE_{soot}}{dt} + \dot{Q}$$

$$\Downarrow \text{from continuity}$$

$$V(1-\varphi) \sum_i \dot{s}_i W_i \sum_k Y_k e_k + m \sum_k \frac{dY_k}{dt} e_k + m \sum_k Y_k \frac{de_k}{dt} = -\frac{dE_{soot}}{dt} + \dot{Q}$$

$$\Downarrow \text{from species}$$

$$V(1-\varphi) \sum_i \dot{s}_i W_i \sum_k Y_k e_k + m \sum_k \frac{1}{\rho} \left[(\dot{\omega}_k + \dot{s}_k) W_k - Y_k \sum_i \dot{s}_i W_i \right] e_k + m \sum_k Y_k \frac{de_k}{dt} = -\frac{dE_{soot}}{dt} + \dot{Q}$$

$$\Downarrow Y_k \frac{de_k}{dt} = Y_k c_{c,k} \frac{dT}{dt}$$

$$\Downarrow \sum_k Y_k c_{c,k} = c_p$$

$$V(1-\varphi) \sum_i \dot{s}_i W_i \sum_k Y_k e_k + m \sum_k \frac{1}{\rho} \left[(\dot{\omega}_k + \dot{s}_k) W_k - Y_k \sum_i \dot{s}_i W_i \right] e_k + m c_v \frac{dT}{dt} = -\frac{dE_{soot}}{dt} + \dot{Q}$$

$$\Downarrow \frac{dE_{soot}}{dt} = \left(\rho_{soot} c_{v,soot} \varphi \frac{dT}{dt} - (1-\varphi) \sum_i \dot{s}_i W_i e_{soot} \right) V$$

$$V(1-\varphi) \sum_i \dot{s}_i W_i \sum_k Y_k e_k + m \sum_k \frac{1}{\rho} \left[(\dot{\omega}_k + \dot{s}_k) W_k - Y_k \sum_i \dot{s}_i W_i \right] e_k + m c_v \frac{dT}{dt} =$$

$$- \left(\rho_{soot} c_{v,soot} \varphi \frac{dT}{dt} - (1-\varphi) \sum_i \dot{s}_i W_i e_{soot} \right) V + \dot{Q}$$

$$\Downarrow m = \rho V(1-\varphi)$$

$$\begin{aligned}
& V(1-\varphi) \sum_i \dot{s}_i W_i \sum_k Y_k e_k + V(1-\varphi) \sum_k (\dot{\omega}_k + \dot{s}_k) W_k e_k - V(1-\varphi) \sum_k Y_k e_k \sum_i \dot{s}_i W_i \\
& + \rho V(1-\varphi) c_v \frac{dT}{dt} = - \left(\rho_{soot} c_{v,soot} \varphi \frac{dT}{dt} - (1-\varphi) \sum_i \dot{s}_i W_i e_{soot} \right) V + \dot{Q}
\end{aligned}$$

$$\Downarrow \text{Eliminating } V(1-\varphi) \sum_i \dot{s}_i W_i \sum_k Y_k e_k$$

$$\Downarrow \times 1/V$$

$$\begin{aligned}
(1-\varphi) \sum_k (\dot{\omega}_k + \dot{s}_k) W_k e_k + \rho(1-\varphi) c_v \frac{dT}{dt} &= -\rho_{soot} c_{v,soot} \varphi \frac{dT}{dt} + \\
& (1-\varphi) \sum_i \dot{s}_i W_i e_{soot} + \dot{Q}
\end{aligned}$$

$$\Downarrow$$

$$(\rho(1-\varphi) c_v + \rho_{soot} c_{v,soot} \varphi) \frac{dT}{dt} = -(1-\varphi) \sum_k e_k (\dot{\omega}_k + \dot{s}_k) W_k + (1-\varphi) \sum_i \dot{s}_i W_i e_{soot} + \frac{\dot{Q}}{V}$$

$$\Downarrow$$

$$\begin{aligned}
\frac{dT}{dt} &= \frac{1}{\rho(1-\varphi) c_v + \rho_{soot} c_{v,soot} \varphi} \left[-(1-\varphi) \sum_k e_k (\dot{\omega}_k + \dot{s}_k) W_k \right. \\
& \left. + (1-\varphi) \sum_i \dot{s}_i W_i e_{soot} + \frac{\dot{Q}}{V} \right] \tag{A.3}
\end{aligned}$$

A.1.4 Soot Variables

The derivation of equations for soot variables can be accomplished similar to species evolution.

$$\frac{d}{dt}(m\psi) = \rho V(1-\varphi) S_\psi$$

$$\Downarrow$$

$$\frac{d}{dt}(\rho V(1-\varphi)\psi) = \rho V(1-\varphi) S_\psi$$

$$\Downarrow \times 1/V$$

$$\rho(1-\varphi) \frac{d\psi}{dt} + \psi \frac{d}{dt}(\rho(1-\varphi)) = \rho(1-\varphi) S_\psi$$

$$\Downarrow \text{from continuity}$$

$$\begin{aligned}
\rho(1-\varphi) \frac{d\psi}{dt} + \psi V(1-\varphi) \sum_i \dot{s}_i W_i &= \rho(1-\varphi) S_\psi \\
\Downarrow \times \frac{1}{\rho(1-\varphi)} \\
\frac{d\psi}{dt} &= S_\psi - \frac{1}{\rho} \left[\psi \sum_i \dot{s}_i W_i \right]
\end{aligned} \tag{A.4}$$

A.2 Plug Flow Reactor

A.2.1 Continuity

The gas flow that passes through the cross-section of a differential element along the flow reactor is described as:

$$\begin{aligned}
\rho u A(1-\varphi) \big|_{z+dz} - \rho u A(1-\varphi) \big|_z &= A dz (1-\varphi) \sum_i \dot{s}_i W_i \\
\Downarrow \\
\rho u(1-\varphi) A &= A dz (1-\varphi) \sum_i \dot{s}_i W_i \\
\Downarrow \\
\frac{d}{dz} (\rho u(1-\varphi)) &= (1-\varphi) \sum_i \dot{s}_i W_i
\end{aligned} \tag{A.5}$$

A.2.2 Species

$$\begin{aligned}
\frac{d}{dz} (m_k) &= (1-\varphi) (\dot{\omega}_k + \dot{s}_k) W_k \\
\Downarrow \\
\frac{d}{dz} (\rho u(1-\varphi) Y_k) &= (1-\varphi) (\dot{\omega}_k + \dot{s}_k) W_k \\
\Downarrow \\
\rho u(1-\varphi) \frac{dY_k}{dz} + Y_k \frac{d}{dz} (\rho u(1-\varphi)) &= (1-\varphi) (\dot{\omega}_k + \dot{s}_k) W_k \\
\Downarrow \text{ from Equation (A.5)} \\
\rho u(1-\varphi) \frac{dY_k}{dz} + Y_k (1-\varphi) \sum_i \dot{\omega}_i W_i &= (1-\varphi) (\dot{\omega}_k + \dot{s}_k) W_k \\
\Downarrow \times 1/(\rho(1-\varphi)) \\
\frac{dY_k}{dz} &= \frac{1}{\rho u(1-\varphi)} \left[(1-\varphi) (\dot{\omega}_k + \dot{s}_k) W_k - Y_k (1-\varphi) \sum_i \dot{s}_i W_i \right]
\end{aligned} \tag{A.6}$$

A.2.3 Energy

$$\frac{d}{dz} (\rho u (1 - \varphi) h) + \frac{d}{dz} (\rho u \varphi h_{soot}) = \dot{q}'$$

$$\Downarrow$$

$$\frac{dh}{dz} (\rho u (1 - \varphi)) + h \frac{d}{dz} (\rho u (1 - \varphi)) + \frac{d}{dz} (\rho u \varphi) h_{soot} + \frac{dh_{soot}}{dz} \rho u \varphi = \dot{q}'$$

$$\Downarrow h = \sum_k Y_k h_k$$

$$\rho u (1 - \varphi) \frac{d}{dz} \left(\sum_k Y_k h_k \right) + h \frac{d}{dz} (\rho u (1 - \varphi)) + \frac{d}{dz} (\rho u \varphi) h_{soot} + \frac{dh_{soot}}{dz} \rho u \varphi = \dot{q}'$$

$$\Downarrow$$

$$\rho u (1 - \varphi) \sum_k \frac{dY_k}{dz} h_k + \rho u (1 - \varphi) \sum_k \frac{dh_k}{dz} Y_k + h \frac{d}{dz} (\rho u (1 - \varphi)) + \frac{d}{dz} (\rho u \varphi) h_{soot} + \frac{dh_{soot}}{dz} \rho u \varphi = \dot{q}'$$

$$\Downarrow \text{from Equation (A.5) \& (A.6)}$$

$$\rho u (1 - \varphi) \sum_k \frac{1}{\rho u} \left[(\dot{\omega}_k + \dot{s}_k) W_k - Y_k \sum_i \dot{s}_i W_i \right] h_k + \rho u (1 - \varphi) \sum_k \frac{dh_k}{dz} Y_k +$$

$$h \frac{d}{dz} \left((1 - \varphi) \sum_i \dot{s}_i W_i \right) + \frac{d}{dz} (\rho u \varphi) h_{soot} + \frac{dh_{soot}}{dz} \rho u \varphi = \dot{q}'$$

$$\Downarrow \frac{dh_k}{dz} = c_{p,k} \frac{dT}{dz}$$

$$\Downarrow \sum_k Y_k c_{p,k} = c_p$$

$$\Downarrow \frac{dh_{soot}}{dz} = c_{p,soot} \frac{dT}{dz}$$

$$(1 - \varphi) \sum_k \left[(\dot{\omega}_k + \dot{s}_k) W_k - Y_k \sum_i \dot{s}_i W_i \right] h_k + \rho u (1 - \varphi) c_p \frac{dT}{dz} + h (1 - \varphi) \sum_i \dot{s}_i W_i$$

$$+ \frac{d}{dz} (\rho u \varphi) h_{soot} + c_{p,soot} \frac{dT}{dz} \rho u \varphi = \dot{q}'$$

$$\Downarrow$$

$$(1 - \varphi) \sum_k [(\dot{\omega}_k + \dot{s}_k) W_k] h_k + \rho u (1 - \varphi) c_p \frac{dT}{dz} - (1 - \varphi) \sum_i \dot{s}_i W_i h_{soot} + c_{p,soot} \frac{dT}{dz} \rho u \varphi = \dot{q}'$$

$$\Downarrow$$

$$\left[\rho u (1 - \varphi) c_p + \rho u \varphi c_{p,soot} \right] \frac{dT}{dz} + (1 - \varphi) \sum_k [(\dot{\omega}_k + \dot{s}_k) W_k] h_k - (1 - \varphi) \sum_i \dot{s}_i W_i h_{soot} = \dot{q}'$$

$$\Downarrow$$

$$\frac{dT}{dz} = \frac{1}{\rho u (1 - \varphi) c_p + \rho u \varphi c_{p,soot}} \left[- (1 - \varphi) \sum_k (\dot{\omega}_k + \dot{s}_k) W_k h_k + (1 - \varphi) \sum_i \dot{s}_i W_i h_{soot} + \dot{q}' \right]$$

A.3 Perfectly Stirred Reactor

A.3.1 Continuity

The mass conservation for the partially stirred reactor can be written as:

$$\frac{dm}{dt} = \dot{m}_{in} - \dot{m}_{out} + V (1 - \varphi) \sum_i \dot{s}_i W_i \quad (\text{A.7})$$

A.3.2 Species

$$\frac{d}{dt} (m_k) = \dot{m}_{in} Y_k^* - \dot{m}_{out} Y_k + V (1 - \varphi) (\dot{\omega}_k + \dot{s}_k) W_k$$

$$\Downarrow m_k = m Y_k$$

$$Y_m \frac{dm}{dt} + m (Y_k) = \dot{m}_{in} Y_k^* - \dot{m}_{out} Y_k + V (1 - \varphi) (\dot{\omega}_k + \dot{s}_k) W_k$$

$$\Downarrow \text{from Equation A.7}$$

$$\left(\dot{m}_{in} - \dot{m}_{out} + V (1 - \varphi) \sum_i \dot{s}_i W_i \right) Y_k + \frac{dY_k}{dt} m = \dot{m}_{in} Y_k^* - \dot{m}_{out} Y_k + V (1 - \varphi) (\dot{\omega}_k + \dot{s}_k) W_k$$

$$\Downarrow$$

$$V (1 - \varphi) Y_k \sum_i \dot{s}_i W_i + \frac{dY_k}{dt} m = \dot{m}_{in} (Y_k^* - Y_k) + V (1 - \varphi) (\dot{\omega}_k + \dot{s}_k) W_k$$

$$\Downarrow$$

$$\frac{dY_k}{dt} \rho V (1 - \varphi) = \dot{m}_{in} (Y_k^* - Y_k) + V (1 - \varphi) (\dot{\omega}_k + \dot{s}_k) W_k - V (1 - \varphi) Y_k \sum_i \dot{s}_i W_i$$

$$\Downarrow$$

$$\frac{dY_k}{dt} = \frac{\dot{m}_{in}}{\rho V (1 - \varphi)} (Y_k^* - Y_k) + \frac{1}{\rho} (\dot{\omega}_k + \dot{s}_k) W_k - \frac{1}{\rho} Y_k \sum_i \dot{s}_i W_i \quad (\text{A.8})$$

A.3.3 Energy

$$\frac{dH}{dt} = \dot{m}_{in} h^* - \dot{m}_{out} h - \frac{dH_{soot}}{dt} + \dot{Q}$$

$$\Downarrow H = mh$$

$$\frac{dm}{dt} h + m \frac{dh}{dt} = \dot{m}_{in} h^* - \dot{m}_{out} h - \frac{dH_{soot}}{dt} + \dot{Q}$$

$$\Downarrow \text{from Equation A.7}$$

$$\left(\dot{m}_{in} - \dot{m}_{out} + V(1 - \varphi) \sum_i \dot{s}_i W_i \right) h + m \frac{dh}{dt} = \dot{m}_{in} h^* - \dot{m}_{out} h - \frac{dH_{soot}}{dt} + \dot{Q}$$

$$\Downarrow$$

$$V(1 - \varphi) h \sum_i \dot{s}_i W_i + m \frac{dh}{dt} = \dot{m}_{in} (h^* - h) - \frac{dH_{soot}}{dt} + \dot{Q}$$

$$\Downarrow$$

$$m \frac{dh}{dt} = \dot{m}_{in} (h^* - h) - V(1 - \varphi) h \sum_i \dot{s}_i W_i - \frac{dH_{soot}}{dt} + \dot{Q}$$

$$\Downarrow h = \sum Y_k h_k$$

$$m \sum \frac{dY_k}{dt} h_k + m \sum \frac{dh_k}{dt} Y_k = \dot{m}_{in} (h^* - h) - V(1 - \varphi) h \sum_i \dot{s}_i W_i - \frac{dH_{soot}}{dt} + \dot{Q}$$

$$\Downarrow \text{from Equation A.8}$$

$$m \sum \left(\frac{\dot{m}_{in}}{\rho V (1 - \varphi)} (Y_k^* - Y_k) + \frac{1}{\rho} (\dot{\omega}_k + \dot{s}_k) W_k - \frac{1}{\rho} Y_k \sum_i \dot{s}_i W_i \right) h_k + m \sum c_{p,k} \frac{dT}{dt} Y_k =$$

$$\dot{m}_{in} (h^* - h) - V(1 - \varphi) h \sum_i \dot{s}_i W_i - \frac{dH_{soot}}{dt} + \dot{Q}$$

$$\Downarrow m = \rho V (1 - \varphi)$$

$$\dot{m}_{in} \sum (Y_k^* - Y_k) h_k + V(1 - \varphi) \sum (\dot{\omega}_k + \dot{s}_k) W_k h_k + m c_p \frac{dT}{dt} = \dot{m}_{in} (h^* - h) - \frac{dH_{soot}}{dt} + \dot{Q}$$

$$\Downarrow$$

$$\begin{aligned} \dot{m}_{in} \sum (Y_k^* - Y_k) h_k + V(1 - \varphi) \sum (\dot{\omega}_k + \dot{s}_k) W_k h_k + m c_p \frac{dT}{dt} &= \dot{m}_{in} (h^* - h) \\ &- \left(\rho_{soot} c_{p,soot} \varphi V \frac{dT}{dt} - (1 - \varphi) V \sum_i \dot{s}_i W_i h_{soot} \right) + \dot{Q} \end{aligned}$$

$$\Downarrow$$

$$\begin{aligned} \dot{m}_{in} \sum (Y_k^* - Y_k) h_k + V (1 - \varphi) \sum (\dot{\omega}_k + \dot{s}_k) W_k h_k + m c_p \frac{dT}{dt} = \dot{m}_{in} (h^* - h) \\ - \left(\rho_{soot} c_{p,soot} \varphi V \frac{dT}{dt} - (1 - \varphi) V \sum_i \dot{s}_i W_i h_{soot} \right) + \dot{Q} \end{aligned}$$

$$\Downarrow m = \rho V (1 - \varphi)$$

$$\Downarrow \times 1/V$$

$$\begin{aligned} \dot{m}_{in} \sum (Y_k^* - Y_k) h_k + V (1 - \varphi) \sum (\dot{\omega}_k + \dot{s}_k) W_k h_k + \rho V (1 - \varphi) c_p \frac{dT}{dt} = \\ \dot{m}_{in} (h^* - h) - \left(\rho_{soot} c_{p,soot} \varphi V \frac{dT}{dt} - (1 - \varphi) V \sum_i \dot{s}_i W_i h_{soot} \right) + \dot{Q} \end{aligned}$$

$$\Downarrow$$

$$\begin{aligned} (\rho (1 - \varphi) c_p + \rho_{soot} c_{p,soot} \varphi) \frac{dT}{dt} = \frac{\dot{m}_{in}}{V} (h^* - h) - \frac{\dot{m}_{in}}{V} \sum (Y_k^* - Y_k) h_k \\ - (1 - \varphi) \sum (\dot{\omega}_k + \dot{s}_k) W_k h_k + (1 - \varphi) \sum_i \dot{s}_i W_i h_{soot} + \frac{\dot{Q}}{V} \end{aligned}$$

$$\Downarrow$$

$$\begin{aligned} \frac{dT}{dt} = \frac{1}{\rho (1 - \varphi) c_p + \rho_{soot} c_{p,soot} \varphi} \left[\frac{\dot{m}_{in}}{V} (h^* - h) - \frac{\dot{m}_{in}}{V} \sum (Y_k^* - Y_k) h_k - (1 - \varphi) \sum (\dot{\omega}_k + \dot{s}_k) W_k h_k \right. \\ \left. + (1 - \varphi) \sum_i \dot{s}_i W_i h_{soot} + \frac{\dot{Q}}{V} \right] \end{aligned} \quad (\text{A.9})$$